

1
2
3
4
5
6
7
8
9
10
11

Advecting Superspecies: Efficiently Modeling Transport of Organic Aerosol with a Mass-Conserving Dimensionality Reduction Method

Patrick Obin Sturm^{1,3}, Astrid Manders², Ruud Janssen², Arjo Segers²,
Anthony S. Wexler^{1,4}, Hai Xiang Lin^{3,5}

¹Air Quality Research Center, University of California, Davis, CA, USA

²Department of Climate, Air and Sustainability, TNO, Utrecht, the Netherlands

³Delft Institute of Applied Mathematics, Delft University of Technology, Delft, the Netherlands

⁴Departments of Mechanical and Aerospace Engineering, Civil and Environmental Engineering, and Land,

Air and Water Resources, University of California, Davis, CA, USA

⁵Institute of Environmental Sciences, Leiden University, the Netherlands

12
13
14
15
16
17
18

Key Points:

- We develop a data-driven method to find a reduced-dimension set of superspecies representing tracers in a chemical transport model
- This method is designed to be physically consistent, preserving information on phase and conserving mass to machine precision
- Advecting the superspecies accelerates the advection operator by a factor of 1.5 to 1.8

Corresponding author: Patrick Obin Sturm, posturm@ucdavis.edu

19 **Abstract**

20 The chemical transport model LOTOS-EUROS uses a volatility basis set (VBS)
21 approach to represent the formation of secondary organic aerosol (SOA) in the
22 atmosphere. Inclusion of the VBS approximately doubles the dimensionality of
23 LOTOS-EUROS and slows computation of the advection operator by a factor of
24 two. This complexity limits SOA representation in operational forecasts. We develop
25 a mass-conserving dimensionality reduction method based on matrix factorization to
26 find latent patterns in the VBS tracers that correspond to a smaller set of
27 superspecies. Tracers are reversibly compressed to superspecies before transport, and
28 the superspecies are subsequently decompressed to tracers for process-based SOA
29 modeling. This physically interpretable data-driven method conserves the total
30 concentration and phase of the tracers throughout the process. The superspecies
31 approach is implemented in LOTOS-EUROS and found to accelerate the advection
32 operator by a factor of 1.5 to 1.8. Concentrations remain numerically stable over
33 model simulation times of two weeks, including simulations at higher spatial
34 resolutions than the data-driven models were trained on. The reversible
35 compression of VBS tracers enables detailed, process-based SOA representation in
36 LOTOS-EUROS operational forecasts in a computationally efficient manner. Beyond
37 this case study, the physically consistent data-driven approach developed in this
38 work enforces conservation laws that are essential to other Earth system modeling
39 applications, and generalizes to other processes where computational benefit can be
40 gained from a two-way mapping between detailed process variables and their
41 representation in a reduced-dimensional space.

42 **Plain Language Summary**

43 The chemical composition of the atmosphere is a complex system involving
44 many physical processes. Computer models can be used to improve our
45 understanding of how these processes interact, as well as simulate hypothetical
46 scenarios to support scientifically-informed climate and air quality policies. However,
47 complicated models with many variables can take a lot of time to run. The
48 LOTOS-EUROS model spends a large fraction of time and computational resources
49 on simulating the transport of chemical species, like particulate matter, by wind. We
50 combine data-driven approaches with domain knowledge to reduce the number of
51 variables while ensuring essential properties are conserved: we model representative
52 combinations of chemical species that are transported all at once, rather than
53 transport each species individually. This leads to faster and cheaper simulations
54 without loss of scientific detail or internal consistency.

1 Introduction

Vast amounts of computational resources are required to model phenomena in the Earth sciences. This includes complex models of atmospheric composition that couple a large number of properties and processes (Brasseur & Jacob, 2017). Data-driven approaches, including machine learning (ML), are an emerging set of techniques for decreasing the computational burden of Earth System Models (ESMs) by using more efficient parameterizations, but have documented challenges such as unstable error growth and physical inconsistency when predicted recurrently (Kelp et al., 2018) or when interacting with other processes in the context of larger models (Rasp et al., 2018; Brenowitz & Bretherton, 2019). One approach towards data-driven ML models that can stably interact with other model processes is online training: parameter optimization of neural network surrogates while running the entire model (Rasp, 2020; Kelp et al., 2022).

Other recent efforts have aimed to constrain data-driven approaches using domain knowledge to ensure physically consistent results. One strategy for physically consistent data-driven models reposes the learning targets: rather than estimate important properties or their tendencies, instead estimate fluxes between the properties. The fluxes can then be related to tendencies in a way that balances mass, energy, or atoms (Sturm & Wexler, 2020; Yuval et al., 2021; Sturm & Wexler, 2022). Custom neural network architectures can also obey conservation laws by incorporating hard constraints in their hidden layers (Beucler et al., 2021), such as flux balances (Sturm & Wexler, 2022): this can also improve the physical interpretability of the inner working of neural networks. Though physical consistency is an important result by itself, imposed constraints do not necessarily improve accuracy of such tools beyond adherence to whichever physical law(s) the constraints enforce. For example, Harder et al. (2022) found the accuracy of a neural network surrogate model of aerosol microphysics was not improved when adding a completion constraint during training, where a chosen variable was reassigned to the sum of all other variables' tendencies to conserve mass. However, constraints can be implemented in ways that add domain knowledge to the data-driven algorithm: Sturm and Wexler (2022) found that by adjusting a feed-forward neural network architecture to include a flux-tendency constraint during training, the overall prediction accuracy of chemical species concentrations improved. Kelp et al. (2020) motivated ML model architectures with built-in assumptions about the physical system as a future research direction. In the approach in Sturm and Wexler (2022) the constraint gives information on the graph relational structure of a chemical mechanism, i.e. how different chemical species interact. Recent work toward physically consistent data-driven tools in the Earth sciences, and acknowledgement of their importance (Keller & Evans, 2019; Sturm & Wexler, 2020; Yuval, Pritchard, et al., 2021) has motivated the mass-conserving dimensionality reduction method in this paper.

Within the field of atmospheric chemistry modeling, Kelp et al. (2020) have made progress towards a stable neural network emulating a box model of chemistry and aerosol microphysics processes, through training parameters on the accuracy of multiple future timesteps after predicting in a lower-dimensional latent space. Kelp et al. (2020) pose a future research direction: how the low-dimensional representation of chemical species might interact with other processes, such as advection, in the context of a larger model. The scope of the present study is informed by this direction: we develop and assess a physically consistent data-driven method that compresses the high dimensional set of organic aerosol (OA) tracers to reduce the computational cost of advection in the LOTOS-EUROS chemical transport model (CTM) (Manders et al., 2017). LOTOS-EUROS is a state-of-the-art model that has been compared to the WRF-Chem, CAMx, CMAQ and EMEP

108 models in several international model intercomparison studies such as AQMEII (Im
109 et al., 2015) and EURODELTA-Trends (Colette et al., 2017) and is part of the
110 European Copernicus Atmospheric Monitoring (CAMS) model ensemble. The
111 advection operator consumes a significant amount of wall time in LOTOS-EUROS,
112 from about 20% of total wall time in sequential runs (only chemistry and sometimes
113 deposition calculations take longer) to over 50% of total wall time in parallel runs
114 using domain decomposition. Wall time of advection can double with the inclusion
115 of organic aerosol tracers (Sturm, 2021). Therefore, the current default in
116 LOTOS-EUROS is to include only one passive tracer for organic aerosol, which is
117 one of the reasons for an underestimation of total particulate matter (Timmermans
118 et al., 2022).

119 Organic aerosol forms an important contribution to particulate matter
120 (Jimenez et al., 2009). OA can be emitted to the atmosphere as semi-volatile
121 primary organic aerosol (POA) through various direct sources, including vehicle
122 exhaust, wildfire smoke, and residential wood combustion. OA can also be formed in
123 the atmosphere as secondary organic aerosol (SOA) through gas-phase reactions of
124 volatile organic compounds (VOCs), which tend to form less volatile products:
125 intermediate volatility organic compounds (IVOC) and semi-volatile organic
126 compounds (SVOC), referred to together as siVOC. SVOC can partition appreciably
127 to the particle phase under ambient conditions. Both anthropogenic sources, like
128 industrial activity, and biogenic sources, such as forests, emit precursors of SOA.
129 Another source of SOA is the partial evaporation of POA to siVOCs, which in turn
130 react and partition to form SOA (Robinson et al., 2007). This SOA from evaporated
131 and aged POA is often chemically distinct from POA, showing a higher degree of
132 oxidation (Jimenez et al., 2009), and can be tracked separately in models. SOA can
133 form a significant fraction of the total OA concentration (de Gouw et al., 2005;
134 Heald et al., 2005).

135 Due to the large number of distinct organic species in the atmosphere, organic
136 aerosols are often lumped together into volatility bins according to the magnitude of
137 their saturation vapor pressures (Donahue et al., 2006). This modeling approach is
138 called the volatility basis set (VBS) and accounts for the tendency of compounds to
139 become less volatile as they are oxidized. The partitioning between gas and particle
140 phase in each volatility bin is governed by its corresponding saturation vapor
141 pressure and the total OA concentration. A 2D-VBS extension has been developed
142 that includes oxygen to carbon ratio along another dimension (Jimenez et al., 2009;
143 Donahue et al., 2011), which can account for fragmentation of larger compounds and
144 estimation of hygroscopicity (Jimenez et al., 2009). A 1D-VBS approach is
145 commonly applied in chemical transport models, including separate basis sets for
146 different classes of OA precursors (Bergström et al., 2012; Hayes et al., 2015; Janssen
147 et al., 2017; Jiang et al., 2019). Use of multiple VBS classes enables distinct
148 properties per class and can give insight into different aerosol systems contributing
149 to total OA. Recent SOA modeling work has concentrated on several topics: 1)
150 further specification of IVOC emissions from specific sources like gasoline and diesel
151 (Jathar et al., 2014; Ots et al., 2016; Lu et al., 2020) and biomass burning (Ciarelli
152 et al., 2017; Theodoritsi & Pandis, 2019; Jiang et al., 2019), 2) effect of aerosol
153 water content on OA partitioning (Pye et al., 2017), 3) the role of SVOC deposition
154 (Knote et al., 2015) and 4) other OA formation pathways, such as reactive uptake of
155 isoprene epoxides (Pye et al., 2013; Marais et al., 2016; Nagori et al., 2019). Hodzic
156 et al. (2016) and Pai et al. (2020) provide a global scale synthesis of some of these
157 ideas.

158 The inclusion of such detailed, high-dimensional process-based OA models in
159 3D models is limited by their increased computational burden, for example to
160 chemical transport models like LOTOS-EUROSv2.2.1 (Manders et al., 2017). Next

161 to an implementation with a single passive organic aerosol tracer, LOTOS-EUROS
162 has an implementation with four VBS classes based on the configuration from
163 Bergström et al. (2012).

164 Though this approach does not resemble the modern state of the science as
165 discussed in the previous paragraph, it strikes a balance between complexity and
166 level of realism of OA processes: a four-class VBS approach has a higher level of
167 realism than the two-product model (SORGAM) (Odum 1996, Schell 2001) used by
168 other models in air quality forecasts for Europe (Mircea et al., 2019). New
169 developments tend to increase the complexity of the VBS (e.g. by adding specific
170 basis sets for emission sources such as diesel, gasoline, or biomass burning, or by
171 adding more explicit IVOC oxidation). The current VBS module in LOTOS-EUROS
172 v2.2.1 is not used by default, and when included, significantly increases wall time of
173 simulations. The inclusion of VBS tracers adds computation time to other operators
174 in the model relatively more than OA-specific calculations themselves.

175 Most notably, the high dimensionality caused by adding 58 VBS tracers adds a
176 computational burden to the advection operator in LOTOS-EUROS v2.2.1, which is
177 based on the mixing-ratio conserving scheme in Walcek (2000). When using the VBS
178 module, the number of advected tracers increases from 46 to 104. Model timing
179 experiments in Sturm (2021) found that wall time for the advection operator can
180 double when using the VBS module. Advection is a bulk process and does not
181 perform OA-specific calculations. This motivates dimensionality reduction for a
182 more parsimonious representation of OA in transport processes: we use unsupervised
183 data-driven approaches to find characteristic regimes of VBS tracers, which are used
184 to form lower-dimensional combinations interpreted as superspecies that require
185 fewer transport calculations. Rather than advecting each tracer separately, we
186 instead advect a smaller set of superspecies, which are subsequently mapped back
187 to the OA tracer space after advection.. Constraints are applied when compressing
188 to and decompressing from the reduced-dimension space to conserve mass to
189 machine precision. We compare the linear and additive method of non-negative
190 matrix factorization to a nonlinear and more complex neural network autoencoder,
191 and make a model selection after evaluating several configurations based on
192 reconstruction accuracy and physical consistency. Though demonstrated for
193 compression of OA and related compounds during transport to accelerate air quality
194 forecasts over the European continent, the methods developed in this work
195 generalize to other Earth system applications, enabling use of high-dimensional
196 process models whose variables can be reversibly compressed to a physically
197 consistent reduced-dimension representation for use in other processes.

198 Section 2 outlines the VBS configuration in LOTOS-EUROS and develops four
199 data-driven approaches. These four approaches are tested in Section 3: first, they
200 are trained on the volatility distributions from LOTOS-EUROS model output, then
201 evaluated on reconstruction accuracy of the volatility distributions and physical
202 consistency. One approach from Section 3 is chosen to be implemented in
203 LOTOS-EUROS, with results from various experiments shown in Section 4. More
204 specifically, Section 4 investigates the accuracy of using the superspecies,
205 generalizability of the converged model to other seasons and different spatial
206 resolutions, and corresponding speedup in the 3D model. Section 5 contains a
207 summary of the methods and key results.

208 **2 Methods**

209 This section develops four data-driven approaches to reversibly compress
210 VBS-specific tracers. Section 2.1 describes the VBS approach in LOTOS-EUROS
211 v2.2.1. Section 2.2 summarizes several other methods for tracer compression.

212 Section 2.3 details the model configuration used for experiments, as well as the
 213 model output used to train the various data-driven approaches. Sections 2.4, 2.5,
 214 and 2.6 develop four approaches that are summarized in Section 2.7.

215 2.1 VBS approach in LOTOS-EUROS

216 The chemical transport model LOTOS-EUROS v2.2.1 uses a VBS scheme
 217 visualized in Figure 1 based on Bergström et al. (2012). This scheme has 4 distinct
 218 VBS classes: 1) POA, 2) SOA from siVOCs that are chemically aged after
 219 evaporating from semi-volatile POA emissions, (abbreviated as siSOA), and SOA
 220 from 3) anthropogenic and 4) biogenic gaseous VOCs, abbreviated as aSOA and
 221 bSOA respectively.

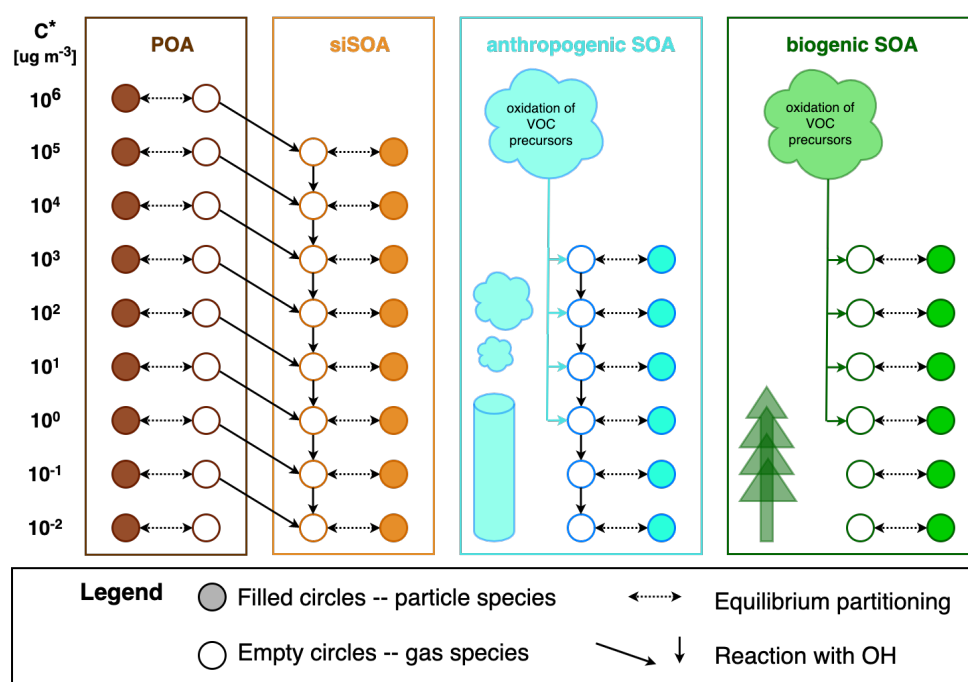


Figure 1. Schematic representation of the VBS approach in LOTOS-EUROS v2.2.1, including the 4 VBS classes with 58 tracers, and their thermodynamic and chemical relationships. This diagram was inspired by the schematic in Shrivastava et al. (2008).

222 Figure 1 provides an overview of the 58 tracers specific to the VBS module.
 223 Primary organic material (POM) emissions are modeled using a 9-bin VBS
 224 approach: the logarithmically distributed bins represent semi- and intermediate-
 225 volatile organics with effective saturation concentrations ranging from 10^{-2} to 10^6
 226 $\mu\text{g m}^{-3}$ at 298 K. The reported mass of primary emissions is distributed over the
 227 lower 4 volatility bins. As in previous work (Shrivastava et al., 2008), an additional
 228 1.5 times this mass is distributed over the highest 5 volatility bins to represent
 229 non-reported intermediate volatility organic compounds (IVOCs). The factor of 1.5
 230 for the VBS in LOTOS-EUROS v2.2.1 is an oversimplification: alternative
 231 approaches exist for estimating IVOC emissions from specific sources (e.g. Jiang et
 232 al., 2019; Ots et al., 2016; Ciarelli et al., 2017; Lu et al., 2020) and further
 233 specification of the VBS in future versions of LOTOS-EUROS could include explicit

234 IVOC emissions per source, adding complexity and underscoring the need for
235 reversible compression for use in transport processes. Only a fraction of the emitted
236 primary material remains in the particle phase: the fraction that evaporates is
237 assumed to be SVOC with effective saturation concentrations on the order of
238 $1 < C^* < 10^3 \mu\text{g m}^{-3}$ or IVOC with saturation concentrations on the order of
239 $10^4 < C^* < 10^6 \mu\text{g m}^{-3}$, defined at 298 K. The S/IVOCs undergo oxidation by the
240 hydroxyl radical OH and enter the distinct siSOA VBS class. As material moves
241 from the POA VBS to the siSOA VBS, it also moves to lower volatility bins, as
242 shown in Figure 1. The total siSOA is represented by an 8-bin VBS using effective
243 saturation concentrations from 10^{-2} to $10^5 \mu\text{g m}^{-3}$ (defined at 298 K). Each bin
244 uses two tracers, one aerosol and one gas, to represent the partitioning: this results
245 in 18 tracers for the POA VBS class and 16 tracers for the siSOA VBS class.
246 Formation of SOA from anthropogenic VOCs is represented with a 6-bin VBS class,
247 defined using effective saturation concentrations of 10^{-2} to $10^3 \mu\text{g m}^{-3}$ at 298 K.
248 This results in 12 tracers (6 in the gas phase and 6 in the particle phase). VOCs
249 such as aromatics, alkenes and alkanes are classified in LOTOS-EUROS as
250 anthropogenic precursors of secondary organic aerosols and upon oxidation are
251 distributed over the 4 highest volatility bins as done by Tsimpidi et al. (2010),
252 linearly interpolating between a low-NO_x and high-NO_x case as originally suggested
253 by Lane et al. (2008).

254 An analogous 6-bin VBS class is used to model SOA formation from the
255 biogenic VOCs in LOTOS-EUROS: monoterpene and isoprene. Yields from biogenic
256 gaseous precursors are distributed over the 4 highest volatility bins according to
257 Tsimpidi et al. (2010), with yields calculated by a branching ratio continuously
258 dependent on NO_x (Lane et al., 2008). Unlike the anthropogenic VBS class, ageing
259 between bins is turned off for the biogenic VBS in LOTOS-EUROS v2.2.1, as in
260 prior work (Murphy & Pandis, 2009; Tsimpidi et al., 2010, 2014; Matsui, 2017).
261 This is informed by the low sensitivity of biogenic SOA concentration to oxidative
262 ageing (Ng et al., 2006; Donahue et al., 2012), thought to arise from fragmentation
263 effects that balance out functionalization effects on volatility (Murphy et al., 2012).
264 For this reason, material never enters the 2 lowest volatility bins in LOTOS-EUROS
265 v2.2.1, rendering the 4 corresponding tracers effectively inert. However, in
266 LOTOS-EUROS v2.2.1 with the VBS module on, these 4 tracers are still dealt with
267 by the model, contributing to the computational burden on processes such as
268 advection.

269 2.2 Tracer compression methods

270 A method for tracer compression for transport in the GEOS-Chem global CTM
271 is given by Liao et al. (2007), where various oxidation products are lumped together
272 by phase and class, and assumed to behave similarly in transport. The relative
273 compositions from each grid cell's previous time step are used to distribute the
274 lumped tracers back to individual products after transport. This can be thought of
275 as compression to a single lumped superspecies with one degree of freedom (the
276 superspecies concentration) and a fixed composition dictated by the grid cell before
277 the advection operator. Another approach for OA tracers given by Matsui (2017)
278 compresses VBS tracers in a global aerosol model from 106 to 26 (a compression
279 factor of approximately 4) by using fewer volatility bins. This effectively lowers the
280 bin resolution and combines material across a wider range of saturation vapor
281 pressures. Analogously, Matsui (2017) converts between high-resolution and
282 low-resolution bins in a sectional aerosol model for use in processes not directly
283 related to aerosols. An example of tracer compression for advection in a 2D-VBS is
284 given by Zhao et al. (2020) who sum tracers along the O:C axis, resulting in a
285 1D-VBS for decreased dimensionality in advection.

286 A partitioning-based compression technique for advection of 1D-VBS tracers
287 could be developed based on partitioning, where the compressed tracers themselves
288 contain all the information needed to decompress to the VBS tracer space without
289 loss of accuracy. This technique advects total concentration for each volatility bin as
290 well as total OA concentration, reducing the 58 phase-specific tracers to 29
291 combined phase tracers and an additional tracer to keep track of total organic
292 aerosol concentration. After advection, total OA along with the saturation vapor
293 concentration determines the partitioning between phase in each volatility bin.
294 However, this theoretical strategy applied to the VBS tracers would yield a
295 compression factor of only approximately 2 (compressing 58 tracers to 30). This
296 would reduce the total number of advected tracers from 104 to 76. We seek a
297 compression technique that can reduce the number of tracers further, leveraging
298 data-driven approaches optimized on a large amount of representative model output,
299 to reversibly compress VBS distributions with minimal accuracy lost.

300 **2.3 Model Configuration and Output**

301 To find latent patterns for a reduced order representation of the 58 VBS
302 tracers, we use LOTOS-EUROS version 2.2.1 (Manders-Groot et al., 2021; Manders
303 et al., 2017) with the optional VBS module. The model is used in its default
304 configuration using 5 levels, the first one being a 25 m surface layer, the second layer
305 reaching the top of the mixing layer, and the other three layers being reservoir layers
306 up to 5 km altitude. The horizontal domain covers 15°W to 35°E and 35-70°N on a
307 lonxlat grid of 0.5x0.25°. This grid is termed the MACC (Monitoring Atmospheric
308 Composition and Change) grid, a predecessor of the current CAMS (Copernicus
309 Atmospheric Monitoring Service). Meteorology is taken from ECMWF IFS 12-hour
310 operational forecasts, using hourly surface values and 3-hour 3D fields interpolated
311 to hourly values. The LOTOS-EUROS advection scheme is based on Walcek (2000).
312 The advection operator does not only refer to bulk horizontal transport by wind, but
313 rather advection in 3 directions: the vertical flux is calculated from the net
314 horizontal flux and continuity. Convection is not implemented as an explicit
315 operator. Instead, the impact of convection is implied by changes in the vertical
316 layer of the model with the first two layers together covering the boundary layer.
317 Other vertical transport is represented by an entrainment and detrainment operator
318 where the vertical structure of the grid is adjusted to mixing layer depth then the
319 pollutant concentrations are linearly interpolated, and a separate vertical diffusion
320 operator. For gas-phase chemistry, a condensed and slightly modified version of
321 CBM-IV is used (Gery et al., 1989). Wet deposition includes in-cloud and
322 below-cloud scavenging as described in Seinfeld and Pandis (2006), deposition of
323 gases is calculated using DEPAC (Zanten et al., 2010), and deposition of particles
324 follows Zhang (2001). The model includes tree-specific biogenic isoprene and terpene
325 emissions as described in Beltman et al (2013) using a high-resolution tree-species
326 database (Köble & Seufert, 2001) that are combined with land cover data from
327 CORINE2000 (EEA, 2005). Anthropogenic emissions are CAMS emissions for 2015
328 (CAMStional air pollutants as delivered in 2018) with a bottom-up estimation for
329 residential wood combustion emissions, providing the best estimate of organic
330 carbon emissions (Denier van der Gon et al., 2015). Wildfire emissions are taken
331 from the MACC global fire assimilation system (Kaiser et al., 2012). Initial and
332 boundary conditions for most species are taken from CAMS near real-time. For
333 organic matter these boundary conditions are not used since they were found to be
334 unrealistically high at some instances. Instead, boundary conditions for OA species
335 were set to zero. With prevailing westerly flow, the assumption of very clean
336 conditions from the western boundary with zero boundary conditions can be
337 justified for most situations and locations not too close to the eastern boundary. In
338 the studied case, boundary conditions act only as a sink.

339 To generate the model output used in this work, we ran short simulations of 14
340 days in the last two weeks of February and July 2018 with 5 days of spin-up, the
341 subsequent 5 days for training data-driven models and the last 4 days for evaluation
342 of the converged data-driven models based on their reconstruction error of the
343 volatility distributions. Evaluation of the simulations with observations is outside
344 the scope of the present paper, as the model is regularly evaluated in model
345 validation reports, as well as CAMS ensemble and model evaluations, and
346 peer-reviewed publications, e.g. Timmermans et al. (2022). With the first 5 days
347 (February 15 through 19) disregarded as spin-up, 9 days were left for training and
348 testing. With hourly output of surface VBS distributions over 216 hours, and 100
349 latitudinal grid lines by 140 longitudinal grid lines on the European MACC grid,
350 there are approximately 3 million multi-dimensional data points for each VBS class.
351 The data points range from 12 dimensional from the anthropogenic and biogenic
352 VBS classes to 16- or 18-dimensional for the siSOA and POA VBS classes
353 respectively. Model output from 5 days over February 20 through 24, approximately
354 1.7 million data points, was used as training data to optimize the parameters of the
355 data-driven models with the objective to compress and reconstruct VBS
356 distributions as accurately as possible. Model output from 4 days over February 25
357 through 28, approximately 1.3 million data points, was used to evaluate how much
358 reconstruction error each approach introduces: this is detailed in Section 3, which
359 concludes with a selection of the most promising approach.

360 Section 4 presents the results of implementing the selected approach in
361 LOTOS-EUROS to compress tracers to superspecies before the advection operator
362 and decompress to the VBS tracer distributions after the advection operator. All 3D
363 experiments in Section 4 are run for periods of 2 weeks, more than double the length
364 of the training time horizon. The operator time splitting step in LOTOS-EUROS is
365 chosen dynamically based on wind conditions to satisfy the Courant-Friedrichs-Lewy
366 criterion (Courant et al., 1967, 1928) varying from 1-10 minutes (Manders et al.,
367 2017) with the advection operator called twice in each time step (Manders-Groot et
368 al., 2021). With the advection operator called at a minimum of 12 times an hour for
369 2 week simulations, the superspecies compression/decompression step is done over
370 4000 times for each grid cell. Grid cells interact with each other via transport
371 processes: over the whole MACC domain with 100 longitudinal grid lines, 140
372 latitudinal grid lines, and 5 levels, superspecies are advected over 280 million times.
373 Section 4 quantifies the effect of advecting superspecies to a baseline run of
374 LOTOS-EUROS advecting all VBS tracers, with model configuration remaining
375 otherwise identical. Also investigated is how well the superspecies optimized on the
376 last 2 weeks of February (winter conditions in Europe) on the MACC grid generalize
377 to a) the last two weeks of July (summer conditions in Europe) with different
378 continental spatial patterns as well as temporal patterns over forested areas and b) a
379 higher-resolution domain of 0.1° by 0.1° used in CAMS forecasting.

380 2.4 Linear Approach

381 A linear approach could be used to project the tracer space into a lower
382 dimensional subspace allowing linear combinations of the tracers to be passed to the
383 advection operator. Principal component analysis is a common linear projection
384 method but is mean-centered and can lead to negative values, which are less readily
385 interpretable as concentrations. Non-negative matrix factorization (NMF), also
386 called positive matrix factorization, is an unsupervised data-driven approach chosen
387 in applications where values must remain non-negative, for example pixel values in
388 image compression (Lee & Seung, 1999) or concentrations in the physical sciences
389 (Paatero & Tapper, 1994). Given a matrix of non-negative data $\mathbf{V} \in \mathbb{R}^{m \times n}$ with m
390 dimensions and n data points, NMF returns two non-negative approximate factors of
391 \mathbf{V} according to an objective function

$$\underset{\mathbf{W}, \mathbf{H}}{\operatorname{argmin}} \|\mathbf{V} - \mathbf{WH}\| \quad \text{s.t.} \quad \mathbf{W}, \mathbf{H} \geq 0 \quad (1)$$

where $\mathbf{W} \in \mathbb{R}_{\geq 0}^{m \times r}$ is a mapping from the m dimensional space to a lower dimensional latent space with r features, and $\mathbf{H} \in \mathbb{R}_{\geq 0}^{r \times n}$ is the latent space representation of each data point. The inequality is interpreted as an element-wise constraint. We use the Frobenius norm in the objective function, which is the default NMF norm in the scikit-learn Python package (Pedregosa et al., 2011). For our application, m is the number of tracers for each class, n the total number of grid cells multiplied by the number of time steps, and r the number of superspecies (a hyperparameter selected in Section 3.1). Each row of \mathbf{V} corresponds to a tracer for each VBS class, and each column the tracer distribution for a given grid cell and time step. \mathbf{H} can be physically interpreted as the concentration of r superspecies representing the tracer concentrations of that VBS class: each column of \mathbf{H} corresponds to the grid cell and time step in \mathbf{V} . \mathbf{W} acts as a mapping from the superspecies representation back to the VBS tracer concentrations: a given column of \mathbf{W} can be physically interpreted as the concentration profile of one superspecies, with each element representing the relative composition of a VBS tracer in that superspecies. We use NMF to converge on a \mathbf{W} for each VBS class that contains superspecies with characteristic volatility distribution shapes. These superspecies are linearly combined in ways that capture the variation of VBS distributions over all grid cells as well as possible. The coefficients determining the linear combination are the concentrations of each superspecies.

NMF operates on a data matrix, handling batches of observations all at once. For our application, compression of current concentrations of VBS tracers $\vec{v} \in \mathbb{R}^m$ in a given grid cell to a lower dimensional space needs to happen with each new time step. For the purpose of speeding computations, it might be counterproductive to perform the NMF algorithm online in every time step. If \mathbf{W} is optimized using equation 1 on sufficiently representative training data, it can be used to decompress a set of superspecies $\vec{h} \in \mathbb{R}^r$ to a set of tracers $\vec{v}_{dec} \in \mathbb{R}^m$ approximating \vec{v} . However, we still need to obtain the superspecies vector \vec{h} . Given a sufficiently representative \mathbf{W} , we can use its Moore-Penrose pseudoinverse $\mathbf{W}^+ \in \mathbb{R}^{r \times m}$ to compress a new set of tracers \vec{v} to a corresponding set of new superspecies \vec{h} . \mathbf{W}^+ may have negative elements for $r > 1$ (more than one superspecies, or degree of freedom), theoretically yielding negative values for superspecies or decompressed tracers. This potential limitation is quantified in section 3.2. Instead of a Moore-Penrose pseudoinverse, a positive-valued compression matrix $\mathbf{B} \in \mathbb{R}_{\geq 0}^{r \times m}$ can be obtained by similar non-negative matrix factorization methods, using the objective function:

$$\underset{\mathbf{B}}{\operatorname{argmin}} \|\mathbf{H} - \mathbf{BV}\|_F^2 \quad \text{s.t.} \quad \mathbf{B} \geq 0 \quad (2)$$

The full approach to obtain non-negative compression and decompression matrices then becomes

1. Given tracer data \mathbf{V} , find \mathbf{H} , \mathbf{W} such that $\mathbf{V} - \mathbf{WH}$ is minimized.
2. Given tracer data \mathbf{V} , and using \mathbf{H} from the previous step, find \mathbf{B} such that $\mathbf{H} - \mathbf{BV}$ is minimized.
3. Use \mathbf{B} to compress subsequent observations of VBS tracers \vec{v} to a non-negative vector of superspecies \vec{h} , and \mathbf{W} to decompress \vec{h} to the original tracer space \vec{v}_{dec} .

436 The compression and decompression matrices \mathbf{B} and \mathbf{W} are optimized for each
437 VBS class, to avoid mixing different classes of OA that have different properties (e.g.
438 molar mass). An important hyperparameter of this approach is r , the size of the
439 latent space (number of superspecies). This can be chosen by constructing an elbow
440 plot of error metrics with varying r , while also considering compression factor and is
441 done in Section 3.1.

442 2.5 Nonlinear Approach

443 We investigate whether a more complicated model than the pair of
444 non-negative matrices is appropriate for compressing VBS tracers. Motivated by the
445 recent success of artificial neural networks (NNs) in emulating models of atmospheric
446 composition (Kelp et al., 2020; Sturm & Wexler, 2022; Schreck et al., 2022), we
447 construct a neural network autoencoder that can reversibly compress the VBS
448 tracers to a latent space. Analogously to section 2.4, the NNs are trained on \mathbf{V} for
449 each VBS class over the entire domain and training time frame, with the goal of
450 applying a single NN parameterization for each VBS class at all grid cells. Neural
451 networks are connected networks of artificial neurons: each neuron calculates a
452 linear combination of its input, adds a bias scalar, and feeds this result to a (usually
453 non-linear) activation function (Marsland, 2014). Neurons performing this operation
454 on the same input in parallel are designated as a layer within the neural network.
455 Neural networks can have multiple such layers: vector output from neuron layers
456 that are not final output of the NN are called hidden layers. A neural network
457 autoencoder attempts to replicate the identity function via compression, where
458 hidden layers compress the input to the NN to a smaller latent space of size r . For
459 our application, the activation function chosen for each neuron is a rectified linear
460 unit that outputs the maximum of its input and zero. This choice of activation
461 function constrains output of both the hidden layer and the NN output to their
462 respective positive half-spaces. In other words, like the non-negative
463 compression/decompression matrices in section 2.4, this activation function ensures
464 concentrations will not go below zero.

465 While matrix multiplication to a lower-dimensional space is also part of the
466 linear approach in Section 2.4, the neural network adds complexity in its parameter
467 space via multiple layers with weight parameters, as well as bias and activation
468 functions between layers of neurons. Such complexity obscures physical
469 interpretation: no one layer of the neural network can represent a set of superspecies
470 with distinct compositions as \mathbf{W} does in NMF. This model should be chosen if it
471 significantly outperforms a linear method using the same size r . As the NNs are
472 compared directly to the linear method, one NN per VBS class is chosen.

473 Training a neural network involves optimizing the coefficients of the linear
474 combination and bias scalar for each perceptron through local minimization
475 methods, often gradient descent. To prevent overfitting of the NNs, dropout layers
476 are used to temporarily remove some neurons during training, and training of NNs is
477 stopped when no further improvement in predictions on a set of validation data
478 (10% of the 5 day training data) after a certain number of passes through the
479 training data is obtained (Li et al., 2020). The neural network models are
480 constructed and trained with the Keras library (Chollet et al., 2015) using a
481 TensorFlow backend (Abadi et al., 2016).

482 2.6 Physically Consistent Models: Conserving Mass and Phase

483 Sections 2.4 and 2.5 developed methods to ensure non-negativity of both the
484 compressed superspecies and decompressed tracers. This section refines the linear
485 method to preserve other physical information: concentration and phase.

486 An advantage of the linear method is that the direction of the decompressed
 487 tracer space is invariant to scaling of the superspecies space. In other words, the
 488 concentration of superspecies can be adjusted without changing the relative
 489 volatility distribution of the decompressed tracers. We can use a scaling factor after
 490 compression to ensure that the total concentration of superspecies is equal to the
 491 total concentration of the tracers for each VBS class. Similarly, after decompression,
 492 we can ensure that the total concentration of decompressed tracers is equal to the
 493 total concentrations of superspecies. This ensures that compression and
 494 decompression neither add nor remove mass. The scaling factor s_{com} after using \mathbf{B}
 495 to compress tracers \vec{v} to the superspecies vector \vec{h} is

$$s_{com} = \frac{\sum_{i=1}^m v_i}{\sum_{j=1}^r h_j} \quad (3)$$

496 After decompression to \vec{v}_{dec} using \mathbf{W} , the decompressed tracers can be scaled
 497 using a factor s_{dec} , where

$$s_{dec} = \frac{\sum_{j=1}^r h_j}{\sum_{i=1}^m v_{dec,i}} \quad (4)$$

498 Despite conserving total concentration of all tracers, the concentration of total
 499 organic aerosol (TOA) may not be conserved due to errors in the mass distribution
 500 over volatility bins after decompression. A variation of this method to conserve TOA
 501 instead of total concentration, as well as an alternative way to conserve total
 502 concentration only using \mathbf{W} from NMF, is explored in Sturm (2021). However, the
 503 compromise of conserving TOA versus total concentration is avoidable by adding
 504 another cross section: creating compression and decompression matrices \mathbf{B} and \mathbf{W}
 505 for each phase as well as VBS class, e.g. one transformation for all biogenic gaseous
 506 VBS tracers and a separate transformation for all biogenic particle tracers. This
 507 phase-specific approach results in eight parameterizations instead of four used in
 508 sections 2.4 and 2.5. The following section gives an overview of all four approaches:
 509 these approaches will be tested on their reconstruction accuracy in Section 3.

510 2.7 Four Approaches

511 The methods developed in sections 2.4 through 2.6 lead to the following four
 512 approaches.

- 513 • **Approach 1:** NMF/Pseudoinverse linear approach: NMF to find an optimal
 514 decompression matrix \mathbf{W} , and use its pseudoinverse (with potentially negative
 515 elements) \mathbf{W}^+ as a compression matrix for each VBS class
- 516 • **Approach 2:** Non-negative matrix factorization: NMF to find an optimal
 517 decompression matrix \mathbf{W} and a non-negative compression matrix \mathbf{B} for each
 518 VBS class
- 519 • **Approach 3:** Non-negative neural network autoencoder: Create a more
 520 complicated neural network with ReLU activation functions in the
 521 superspecies and output layers, for each VBS class
- 522 • **Approach 4:** Mass-conserving, non-negative matrix factorization with phase
 523 specific superspecies: Create \mathbf{W} and a non-negative compression matrix \mathbf{B} , for
 524 each phase in each VBS class

525 Section 3 investigates how well each approach can reconstruct volatility
 526 distributions of all four VBS distributions after compression. We select the most
 527 promising method in Section 3.3 based on reconstruction accuracy and physical
 528 consistency, to be incorporated into a 3D simulation.

529 3 Model Development and Selection

530 The four approaches developed in Section 2.4 through 2.6, and outlined in
 531 Section 2.7, were trained on LOTOS-EUROS model output from February 20th
 532 through 24th using the model configuration detailed in Section 2.3. This section
 533 evaluates the four approaches on their ability to compress and reconstruct the
 534 volatility distributions of model output from a different set of days, February 25th
 535 through 28th. Section 3.1 uses Approach 1, the simplest approach, to investigate
 536 how dimensionality of the latent space r (number of superspecies), inversely related
 537 to compression factor, affects reconstruction accuracy. Section 3.2 deals with
 538 physical consistency: Section 3.2.1 investigates how Approach 1 can lead to negative
 539 concentration values, and motivates the non-negativity constraints in Approaches 2,
 540 3 and 4. Section 3.2.2 demonstrates how Approach 4 conserves mass and phase
 541 when mapping tracers to superspecies and back. Finally, Section 3 compares the
 542 reconstruction error and physical consistency of all four compression approaches and
 543 selects the most promising approach to be implemented in LOTOS-EUROS.

544 3.1 Compression Factor and Accuracy

545 To obtain a sense of error obtained by a maximum compression factor and the
 546 simplest model, we use NMF with a single superspecies ($r = 1$) per VBS class to
 547 obtain a decomposition matrix (in this case a vector) \mathbf{W} and calculate its
 548 pseudoinverse \mathbf{W}^+ to be used for compression. This compression strategy is
 549 evaluated on reconstruction accuracy of test model output of the entire domain and
 550 time period, using average bias and root mean square error (RMSE). While bias is
 551 an indicator of the total material that is introduced or removed artificially by
 552 compression, RMSE is an absolute metric that indicates how accurately the
 553 reconstructed VBS tracers reproduce the volatility distribution. Table 1 shows both
 554 reconstruction error metrics for the tracer set of each class, as well as the
 555 reconstruction bias and RMSE's of total organic aerosol concentration (TOA) and
 556 total organic material (TOM) from summing across VBS classes. The mean
 557 concentrations for each VBS class, as well as TOA and TOM, are included for
 558 comparison. We also include normalized root mean square error (NMRSE) and
 559 normalized mean bias (NMB) calculated by respectively dividing RMSE and bias by
 560 the mean.

Table 1. Test reconstruction error metrics using the NMF/Pseudoinverse approach with 1 superspecies per VBS class.

	Mean [$\mu\text{g m}^{-3}$]	RMSE [$\mu\text{g m}^{-3}$]	Bias [$\mu\text{g m}^{-3}$]	NRMSE [%]	NMB [%]
aVOC	0.0043	0.0021	-3.9×10^{-6}	48.8	0.1
bVOC	0.0262	0.0061	2.9×10^{-4}	23.3	1.1
POA	0.0558	0.0441	-0.0021	79.0	-3.7
siSOA	0.0153	0.0205	6.4×10^{-5}	134.0	0.4
TOA	0.386	0.266	0.094	68.9	24.3
TOM	1.61	0.0978	-0.0328	6.1	-2.1

561 Using one superspecies $r=1$ in Approach 1 leads to high values of RMSE
 562 relative to the mean. Moreover, by the use of a single superspecies the tracers pass
 563 through a linear transformation of rank 1: the concentration distribution over the
 564 volatility bins will always have the same shape, with grid cells and different time steps
 565 differing only in magnitude, as scaled by the superspecies concentration h . This
 566 means any spatiotemporal variability of the distribution shape will be lost after
 567 passing through a single-dimensional superspecies space. More complexity is needed
 568 to capture variation in volatility distribution. This motivates larger matrices that
 569 have more degrees of freedom r , which comes at the cost of compression factor.
 570 Figure 2 visualizes the effect of compression extent on accuracy, using \mathbf{W}^+ to
 571 convert to superspecies and \mathbf{W} to map back to tracers. Reconstruction accuracy is
 572 reported for the set of tracers in each class (both particle and gas) as well as TOA
 573 (total organic aerosol, calculated by summing the concentrations of particle tracers
 574 across classes).

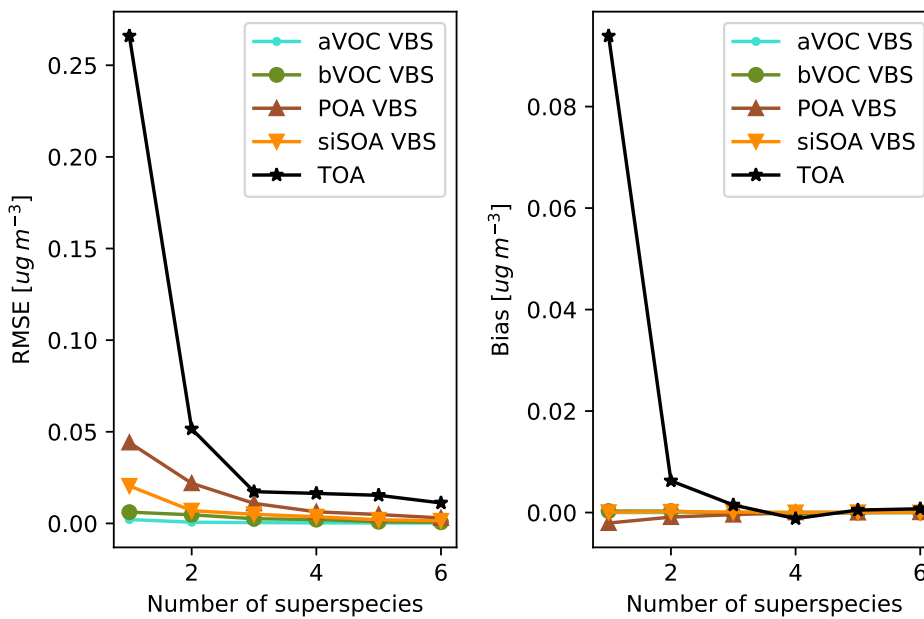


Figure 2. Relationship between the number of superspecies and the RMSE and bias for the 4 VBS classes, as well as TOA. There are diminishing returns in accuracy after 3 superspecies per VBS class.

575 Figure 2 shows RMSE monotonically decreasing with increasing number of
 576 superspecies, with diminishing returns after 3 superspecies. More superspecies to
 577 advect will increase the computational burden of the advection operator in
 578 LOTOS-EUROS without a substantial improvement in RMSE or bias. In light of
 579 the desire to maximize compression factor, the two elbow plots indicate that 3
 580 superspecies strikes a good balance between dimension reduction and accuracy.
 581 Using 3 superspecies per class ranges from a compression factor of 4 (the aVOC and
 582 bVOC basis sets) to 6 (the POA basis set) with a significant improvement in
 583 accuracy from 2 superspecies and minimal improvement in accuracy when using 4 or
 584 more superspecies.

585 Improved accuracy with number of superspecies comes from the increased
 586 degrees of freedom, as each subsequent column of \mathbf{W} adds another basis direction.

587 Each column of \mathbf{W} , when normalized, can also be interpreted as a superspecies of
 588 unit concentration with elements corresponding to composition of VBS tracers. Each
 589 superspecies can also be interpreted as a different regime of organic aerosol, found
 590 through a data-driven method. Multiple superspecies can be combined in different
 591 amounts, corresponding to their concentrations, to form other distributions.

592 3.2 Physical Consistency of Results

593 3.2.1 Motivating Non-negative Constraints

594 Section 2.4 raised the theoretical possibility of obtaining negative
 595 concentrations when using the pseudoinverse \mathbf{W}^+ to compress tracers into
 596 superspecies. Negative elements in \mathbf{W}^+ can lead to negative superspecies. Negative
 597 superspecies concentrations are not directly a problem, as the current advection
 598 scheme in LOTOS-EUROS v2.2.1 is based on that of Walcek (2000), which is able to
 599 handle negative tracer values. However, using the non-negative \mathbf{W} to decompress
 600 negative superspecies concentrations back to the tracer space can lead to negative
 601 tracer values. Here, we quantify this limitation in practice using 3 superspecies.

602 Negative concentrations that are extremely small in magnitude can be
 603 approximated as zero. This tolerance can of course be set to a threshold, for
 604 example $-1 \times 10^{-8} \mu\text{g m}^{-3}$. However, using the test data of the POA VBS as an
 605 example, there are over 4.7 million cases in the test data where a POA VBS tracer is
 606 below $-1 \times 10^{-8} \mu\text{g m}^{-3}$, which is more than 19% of the 24 million values in the
 607 test data for the POA VBS.

608 One could choose a more relative, less arbitrary tolerance: for instance, all
 609 concentrations that are more negative than the magnitude of the corresponding bias
 610 for each VBS. These "significantly negative" concentrations would be negative even
 611 after an additive bias correction. For the POA VBS, there were 855,083 such
 612 concentrations, about 3.5% of the total test data. Using this relative tolerance, other
 613 VBS classes showed even larger proportions of "significantly negative"
 614 concentrations: 4.2%, 5.6%, and 7.0% respectively for the siSOA, aSOA, and bSOA
 615 VBS classes (for the anthropogenic VBS and siSOA VBS, which had positive biases,
 616 the tolerance was chosen to be the negative magnitude of the corresponding bias).

617 Using the pseudoinverse \mathbf{W}^+ for compressing VBS tracers (Approach 1) can
 618 result in a number of significantly negative values when using 3 superspecies per
 619 VBS class, which motivates the development of non-negative compression strategies.
 620 For each VBS class, we find a positive compression matrix \mathbf{B} to replace \mathbf{W}^+ ,
 621 according to the objective function and constraints in equation 2 (Approach 2).

622 We compare this matrix factorization approach (Approach 2) with a neural
 623 network autoencoder (Approach 3) for each VBS class. We construct and train a
 624 5-layer neural network autoencoder with rectified linear unit activation functions in
 625 the superspecies and output layers to ensure non-negativity of both superspecies and
 626 decompressed VBS tracers. In other hidden layers, a sigmoidal activation function,
 627 hyperbolic tangent, is used. In training, a dropout rate of 0.1 is used for every layer
 628 except for the superspecies layer. For the autoencoder of each VBS class, the center
 629 superspecies layer is chosen to have 3 values: the value of this hyperparameter is
 630 chosen for comparison to the linear matrix factorization approach. Section 3.3
 631 compares all four approaches based on how well they reconstruct the VBS tracers
 632 after decompression.

633 3.2.2 Conserving Mass and Phase

634 Section 2.6 proposed a method for conserving total concentration of the VBS
635 tracers in both the superspecies representation and in subsequent reconstruction to
636 decompressed tracers. Approach 4 applies this method to the cross-sections of VBS
637 class and phase (particle or gas) to ensure that the superspecies transformation does
638 not add or remove mass artificially in the gas and particle phases of every class: this
639 results in conservation of total gas concentration, total aerosol concentration, and
640 concentration of total organic material (TOM). Phase-specific superspecies are
641 composed of entirely gas or entirely particle tracers, conserving information on phase
642 while in the latent space representation.

643 Phase-specific superspecies require adding another cross-section, halving the
644 number of tracers to be compressed and decompressed by each pair of \mathbf{B} and \mathbf{W} ,
645 respectively. For this reason, continuing to use 3 superspecies for each phase within
646 each VBS class would reduce the compression factor to slightly over 2.4, not much
647 better than the compression factor of around 2 when using the partitioning-based
648 compression approach. However, using only 1 superspecies per phase per class would
649 fix each corresponding set of tracers to a single shape upon reconstruction, as
650 discussed in section 3.1. To ensure that this method captures spatiotemporal
651 variability of volatility distributions while maintaining a useful compression factor,
652 we choose to use 2 superspecies per phase per VBS class. This design choice results
653 in a compression factor of approximately 3.6. Its accuracy is compared to the other
654 strategies in the model selection process in section 3.3.

655 Figure 3 demonstrates the mass-conserving properties of Approach 4 using
656 representative examples of the primary organic aerosol VBS distribution at two
657 different atmospheric monitoring sites: the Cabauw Experimental Site for
658 Atmospheric Research in the Netherlands, and Mace Head Atmospheric Research
659 Station in Ireland. Mace Head is a more pristine and remote station (O’Dowd et al.,
660 2014). The legend in Figure 3 shows that POA concentration at Cabauw is two
661 orders of magnitude higher than that at Mace Head, $4.984 \mu\text{g m}^{-3}$ compared to
662 $0.032 \mu\text{g m}^{-3}$.

663 Figure 3 compares the primary VBS distribution to the reconstructed primary
664 VBS distributions after mapping to phase-specific superspecies and back again using
665 two sites: Cabauw and Mace Head, as representative examples. Comparing the
666 legends of (a) with (c), it can be seen that total POA concentration, as well as total
667 concentration of tracers in the gas phase, is conserved to machine precision after
668 passing through compression. The same holds for the total concentrations at Mace
669 Head, (b) and (d), at orders of magnitude more dilute. With phase information and
670 concentration conserved, the only source of error caused by compression to
671 superspecies is in the shape of the distribution. This reconstruction error is more
672 apparent at Mace Head in Figure 3 (b) and (d). The reconstructed distribution of
673 Mace Head more closely resembles the constant primary organic emissions profile
674 modeled by LOTOS-EUROS: during training, grid cells with high primary organic
675 emissions are weighted heavily as they tend to have higher aerosol loading. Though
676 the data-driven approaches applied to the primary VBS class are biased to
677 reconstruct the volatility distribution of grid cells with high POA loading, the
678 conservation constraints in Approach 4 ensure that no material will be artificially
679 introduced in more dilute conditions. Though the gas/particle split is not
680 guaranteed to be in equilibrium after reconstruction, the partitioning subroutine
681 (which is not itself a computationally expensive component of the VBS approach)
682 will subsequently determine the gas/particle split.

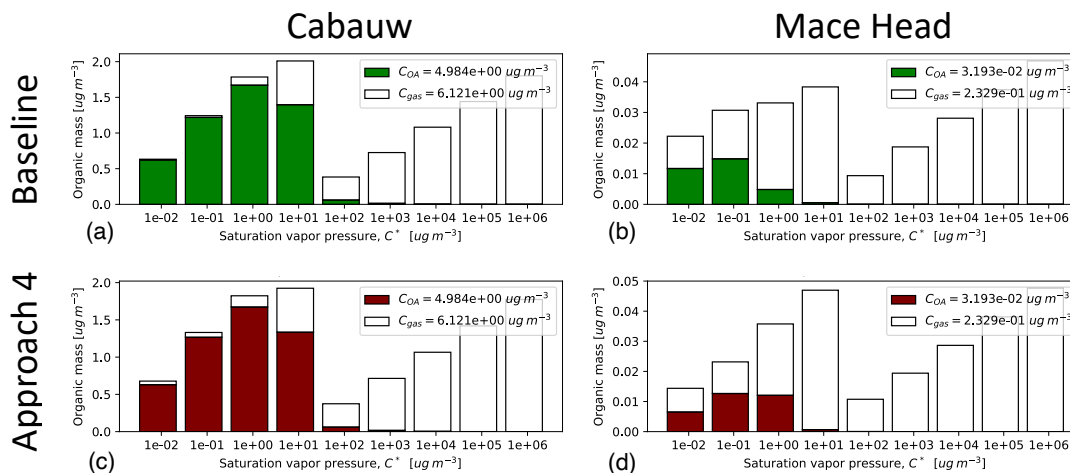


Figure 3. Comparison of the volatility basis set distribution for POA near two sites: Cabauw and Mace Head at a snapshot in time on February 26, 2018. The top row in green shows the distributions as modeled by LOTOS-EUROS at Cabauw (a) and (b) Mace Head. The bottom row in maroon shows the distributions at Cabauw (c) and Mace Head (d) after the non-negative compression/decompression using phase-specific superspecies. Total concentrations are conserved when comparing the legends of the modeled distributions to the reconstructed distributions.

683

3.3 Model Selection

684

In this section, we compare the four approaches described thus far, and make a judgment about the most promising strategy, evaluated on reconstruction accuracy and physical consistency. The selected approach will be implemented in LOTOS-EUROS v2.2.1 to accelerate the advection operator. The four approaches are restated here, including the number of superspecies used.

685

686

687

688

689

690

691

692

693

694

695

696

697

698

699

700

- **Approach 1:** NMF/Pseudoinverse linear approach: NMF to find an optimal decompression matrix \mathbf{W} , and use its pseudoinverse (with negative elements) \mathbf{W}^+ as a compression matrix using 3 superspecies per VBS class
- **Approach 2:** Non-negative matrix factorization: NMF to find an optimal decompression matrix \mathbf{W} and a non-negative compression matrix \mathbf{B} using 3 superspecies per VBS class
- **Approach 3:** Non-negative neural network autoencoder: Create a more complicated neural network with ReLU activation functions in the superspecies and output layers, using 3 superspecies per VBS class
- **Approach 4:** Mass-conserving, non-negative matrix factorization with phase specific superspecies: Create \mathbf{W} , as well as a non-negative compression matrix \mathbf{B} using 2 superspecies per phase per VBS class

701

702

703

Tables 2 and 3 show RMSE and bias of the tracers for each VBS class for the 4 approaches, as well as total organic aerosol (TOA) and total organic material (TOM) concentrations.

704

705

706

Approach 2 uses non-negative \mathbf{B} and \mathbf{W} to linearly combine tracers into three superspecies and shows lower RMSE values than the NN autoencoder in Approach 3, with the exception of TOA concentration. This indicates that matrix factorization

Table 2. Evaluation RMSE of selected approaches. All values reported in $\mu\text{g m}^{-3}$.

	Approach 1	Approach 2	Approach 3	Approach 4
aVOC VBS	4.4×10^{-4}	0.0010	0.0021	0.0011
bVOC VBS	0.0026	0.0078	0.0181	0.0042
POA	0.0109	0.0285	0.0306	0.0142
siSOA	0.0050	0.0086	0.0094	0.0057
TOA	0.0173	0.133	0.101	6.9×10^{-13}
TOM	0.0547	0.240	0.328	1.0×10^{-12}

Table 3. Evaluation bias of selected approaches. All values reported in $\mu\text{g m}^{-3}$.

	Approach 1	Approach 2	Approach 3	Approach 4
aVOC VBS	2.6×10^{-5}	1.2×10^{-4}	-3.9×10^{-4}	2.8×10^{-20}
bVOC VBS	-1.6×10^{-4}	3.8×10^{-4}	-0.0051	-1.6×10^{-16}
POA	-4.2×10^{-4}	0.0050	-0.0075	-8.8×10^{-18}
siSOA	-9.9×10^{-5}	7.7×10^{-4}	-0.0022	1.2×10^{-19}
TOA	0.0015	0.0657	-0.0346	-1.3×10^{-15}
TOM	-0.00763	0.108	-0.237	-2.1×10^{-15}

707 is probably suitable for VBS tracer compression. Using the pseudoinverse \mathbf{W}^+ for
708 compression resulted in lower RMSE for all the VBS classes, but has the critical
709 weakness of producing a significant amount of negative concentrations for
710 superspecies and subsequently reconstructed tracers as explored in Section 3.2.1.
711 Though the phase-specific superspecies approach does not have as low of RMSE for
712 each VBS class as the pseudoinverse approach, it outperforms the other two
713 non-negative approaches. Moreover, it conserves absolute metrics on compression,
714 ensuring that material will stay in each class and each phase, and no material will be
715 added or removed by compression: for this reason, all biases are negligible to
716 machine precision. Preserving information on phase during compression to
717 superspecies has another advantage. This approach can be used in other processes
718 such as dry deposition, which handles particle and gas tracers separately. Because
719 the phase-specific superspecies method (Approach 4) is physically consistent while
720 quite accurate in reconstruction error, and is readily extended to other phase-specific
721 processes, it is chosen for implementation in LOTOS-EUROS v2.2.1.

722 4 Results: Superspecies Implementation in LOTOS-EUROS

723 The phase-specific, matrix factorization superspecies method (Approach 4)
724 chosen in section 3.3 was implemented in LOTOS-EUROS v2.2.1. This section
725 explores the accuracy and speedup of replacing VBS tracers with superspecies in
726 advection, as well as the generalizability of the superspecies to different seasonal
727 conditions and spatial resolutions. Additional tracers for superspecies were added to
728 the LOTOS-EUROS tracer list. Subroutines were added to the VBS module to load
729 the parameterizations, as well as perform the compression and decompression
730 operations. When running with the superspecies method, the subroutines are called
731 in the driver program as follows:

- 732 1. The initialization subroutine loads offline-optimized \mathbf{W} and \mathbf{B} for each phase
733 and class before the time loop starts.

- 734 2. Within the time loop, directly before the call to the advection operator, the
735 compression subroutine is called to map VBS tracers to superspecies
736 concentrations using **B**, overwriting the current superspecies values. The
737 advection operator skips VBS tracers and advects superspecies instead.
738 3. Within the time loop, directly after the call to the advection operator, the
739 decompression routine is called to transform superspecies into VBS tracers
740 using **W**, overwriting previous VBS tracer values.

741 After offline training on data from February 20th through 24th, 2018, the
742 selected superspecies parameterization was loaded into LOTOS-EUROS and used in
743 the advection operator for a run from February 15th through 28th. The results of
744 this run are compared with a control run advecting VBS tracers to directly assess
745 the error from advecting superspecies. Small errors caused by advecting superspecies
746 change subsequent VBS tracer concentrations such that the period of February 20th
747 through 24th differs from the training dataset. In that time period, however,
748 meteorological conditions and other processes independent of the VBS and
749 superspecies parameterization are identical to that of the offline training dataset.
750 For the sake of comparison, the superspecies run and control run are evaluated on
751 February 25th through 28th, even though the superspecies run has the chance to
752 accumulate error and diverge from the control run from the beginning of the
753 simulation on February 15th.

754 Advecting superspecies reproduces the spatial patterns of average TOA across
755 the entire domain. Figure 4 shows average TOA of the control run and the
756 superspecies run, from February 25th through February 28th. This test time period
757 is well into the model run, 10 days after the beginning of the simulation. During this
758 time period and over the entire domain, average bias of TOA of the superspecies run
759 compared to the control run is small and slightly negative, $-0.0095 \mu\text{g m}^{-3}$. Small
760 average bias is not in itself indicative of low error, as positive and negative bias
761 cancellations throughout the domain and time period are possible. RMSE, an
762 absolute metric, was larger at $0.217 \mu\text{g m}^{-3}$. Figure 4 shows total OA, though the
763 VBS classes have partly compensating biases: for example the positive bias in
764 northern Spain was mainly caused by a positive bias from the siSOA class, of which
765 the corresponding gas-phase species have a longer lifetime than those of the POA
766 class. The north of Spain is less densely populated than other parts of the domain
767 and composition is more affected by long-range transport, as are the ocean parts.
768 Back trajectory analysis of this region revealed both stagnant and long-range
769 trajectories for the averaging period (25-28 February), with long-range transport
770 from more polluted areas in the northeast of the domain. Further analysis revealed
771 that for northern Spain siSOA caused a positive bias for TOA. The condensable
772 gases of the siSOA class have a longer lifetime than those of the POA due to
773 differences in their deposition velocities (arising from different Henry coefficient
774 values). However, the general spatial patterns of total OA across the entire domain
775 are preserved when advecting superspecies.

776 **4.1 Seasonal Superspecies**

777 The winter test period from February 25th through 28th directly followed the
778 training test period from February 20th through 24th and had relatively similar
779 conditions to what the superspecies transformation matrices were optimized for. A
780 run in summer from July 20th through August 1st was chosen to assess the
781 robustness of the winter-optimized superspecies to different seasons and weather
782 patterns. Summer conditions differ from winter conditions in Europe for several
783 reasons. One, biogenic precursor gases make up a larger contribution to formation of
784 secondary organic aerosol in the summer, partially due to emissions from forests.
785 Two, average temperatures are higher, affecting the partitioning of the VBS by

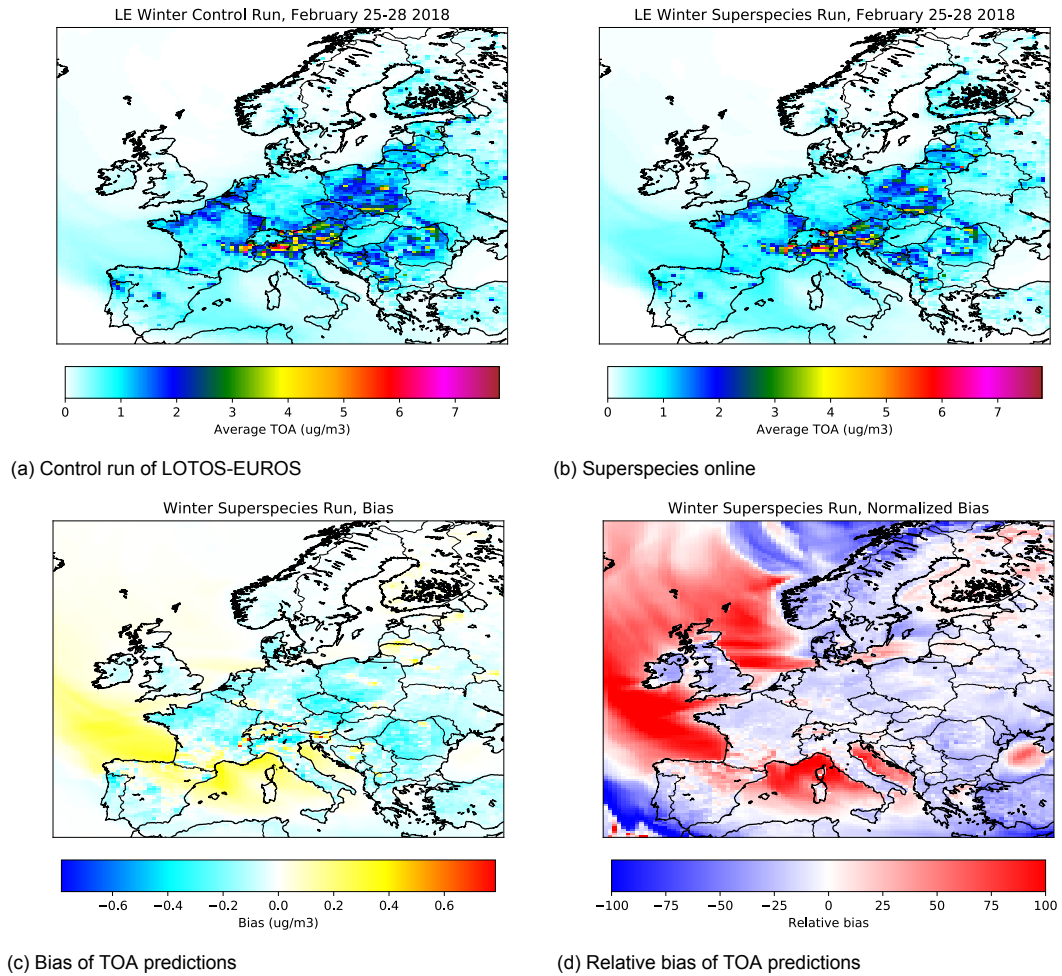


Figure 4. Average TOA for February 25th through 28th 2018, during a 2 week simulation from February 15th through 28th using superspecies matrices optimized offline on winter conditions from February 20th through 24th.

786 changing the volatility basis set values C^* . The different conditions lead to different
 787 modeled compositions of total organic aerosol (TOA). Table 4 compares the modeled
 788 average composition of OA for February 25th through 28th to that for July 29th
 789 through August 1st.

Table 4. Average TOA composition in the control runs for February and July.

OA Type	February	July
aSOA	0.8%	9.5%
bSOA	4.5%	34.8%
POA	61.2%	12.5%
siSOA	33.5%	43.2%

790 Though siSOA is on average the largest component of TOA in the run from
 791 July 29th through August 1st this is not the full picture, and underscores the
 792 importance of bSOA under some conditions. The maximum concentration of surface
 793 siSOA over the entire domain over the entire period from July 29th through August
 794 1st was $15.0 \mu\text{g m}^{-3}$, and 99th percentile $1.3 \mu\text{g m}^{-3}$ compared to the maximum
 795 bSOA concentration of $100.3 \mu\text{g m}^{-3}$ and 99th percentile $9.4 \mu\text{g m}^{-3}$. This indicates
 796 that although siSOA may dominate in background conditions and when TOA is low,
 797 bSOA is the dominant component of TOA in other conditions.

798 **4.1.1 Domain-wide assessment**

799 Figure 5 shows average surface TOA, as predicted by the control run (a), the
 800 run with superspecies advected (b), and the bias and relative bias of the
 801 superspecies run with regards to the control, (c) and (d) respectively. The spatial
 802 patterns of TOA are visually different from the winter conditions in Figure 4.
 803 Primary organic emissions corresponding to POA are often the largest contributor to
 804 winter TOA, and for the time period in Figure 4, TOA is most concentrated in the
 805 Po Valley, Czechia, and Poland. The winter superspecies run is able to recreate
 806 these large regions of high TOA, as well as other smaller but distinct pockets of
 807 TOA, such as Madrid (the most populous city in Spain) and northwestern Portugal,
 808 a region with heavy industrial activity. In contrast, summer TOA is concentrated
 809 around southern Germany, Switzerland, Austria, and Slovenia. Many places in this
 810 region are forested, and contribute to TOA via emission of biogenic precursors of
 811 bSOA. The superspecies run shown in (b) is able to capture these spatial patterns,
 812 but with a strong bias. For this reason, other regions with high biogenic emissions
 813 become visually apparent in (b), such as southern Sweden, Finland Proper, and
 814 northwestern Russia, which are all heavily forested. Woodland regions are accounted
 815 for in LOTOS-EUROS via land use maps and tree-species emissions (Manders et al.,
 816 2017).

817 The superspecies optimized on winter conditions and tested on a 2 week run in
 818 July show a large positive bias over the areas with high average TOA, especially
 819 heavily forested regions. RMSE for TOA over the whole domain and time period is
 820 $2.12 \mu\text{g m}^{-3}$, with an average bias of $0.321 \mu\text{g m}^{-3}$. RMSE of the tracers from the
 821 biogenic VBS for all times and grid cells is $0.66 \mu\text{g m}^{-3}$, an order of magnitude
 822 higher than tracers from the other VBS classes: the class of tracers with the next
 823 highest RMSE value is the siSOA VBS class, at $0.062 \mu\text{g m}^{-3}$. The average bSOA
 824 bias (bias of total biogenic aerosol neglecting gaseous tracers) is $0.068 \mu\text{g m}^{-3}$, three
 825 orders of magnitude smaller than the maximum bSOA bias of $82.9 \mu\text{g m}^{-3}$.
 826 Overestimation of bSOA in the superspecies run under some conditions is likely due
 827 to errors in decompression, artificially shifting mass to lower volatility bins.
 828 However, the large positive bias in parts of the domain indicate that this tendency
 829 to overestimate bSOA only happens in certain conditions: namely, forested regions.
 830 The following section analyzes one grid cell in a forested region, and finds additional
 831 temporal patterns where bSOA is significantly overestimated, leading to
 832 overestimation of TOA.

833 **4.1.2 Case Study: Summer Night in a Forest**

834 We choose a single grid cell over a forested area to investigate the superspecies
 835 tendency to overestimate bSOA. We study the LOTOS-EUROS grid cell containing
 836 the Schönbuch Natural Reserve in southwest Germany, which is 156 square
 837 kilometers and 85% forested. Figure 6a shows the temporal variation of TOA in the
 838 Schönbuch from July 29th through August 1st. This overestimation systematically
 839 occurs at night, with the night of July 30th to July 31st a particularly high TOA
 840 event showing the highest bias.

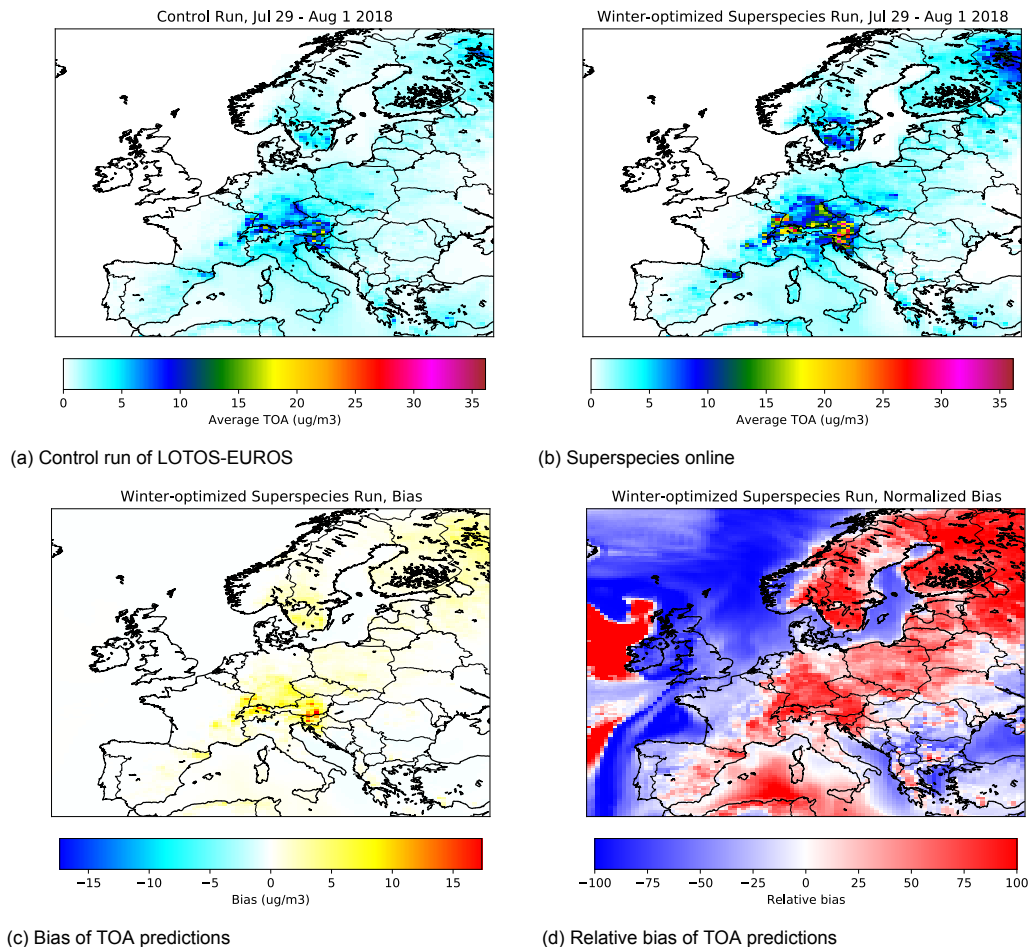


Figure 5. Average TOA for July 29th through August 1st 2018, during a 2 week simulation from July 19th through August 1st using superspecies matrices optimized offline on winter conditions from February 20th through 24th.

841 Examining Figure 6a, the peak overestimation occurs at 05:00 on July 31st and
 842 overestimates total bSOA with a factor between 2 and 2.5 times that of the control
 843 run. The superspecies run has a bSOA concentration of $32.9 \mu\text{g m}^{-3}$, which
 844 comprises 99% of total OA concentration for that grid cell and time. The control
 845 run concentration of bSOA is $14.1 \mu\text{g m}^{-3}$, about 95% of TOA for that simulation.
 846 By 09:00 on July 31st, both runs return to a total bSOA concentration of less than
 847 $3.5 \mu\text{g m}^{-3}$. This night episode of high bSOA contains the largest overpredictions
 848 for that particular grid cell in the whole time period. However, it is illustrative of a
 849 failure mode of the winter-optimized superspecies to capture the total concentration
 850 of bSOA, and ultimately TOA due to the importance of bSOA contributions in this
 851 example. The spatial patterns and temporal patterns of the superspecies run
 852 compared to the control run show that the superspecies are limited in their ability
 853 to model conditions over forested areas on summer nights.

854 Given that winter-optimized superspecies showed limitations in capturing high
 855 bSOA events over forested areas at night, we investigate whether superspecies
 856 optimized on summer conditions and implemented online reproduce high bSOA
 857 conditions with more accuracy. Approach 4 was applied to model output from July

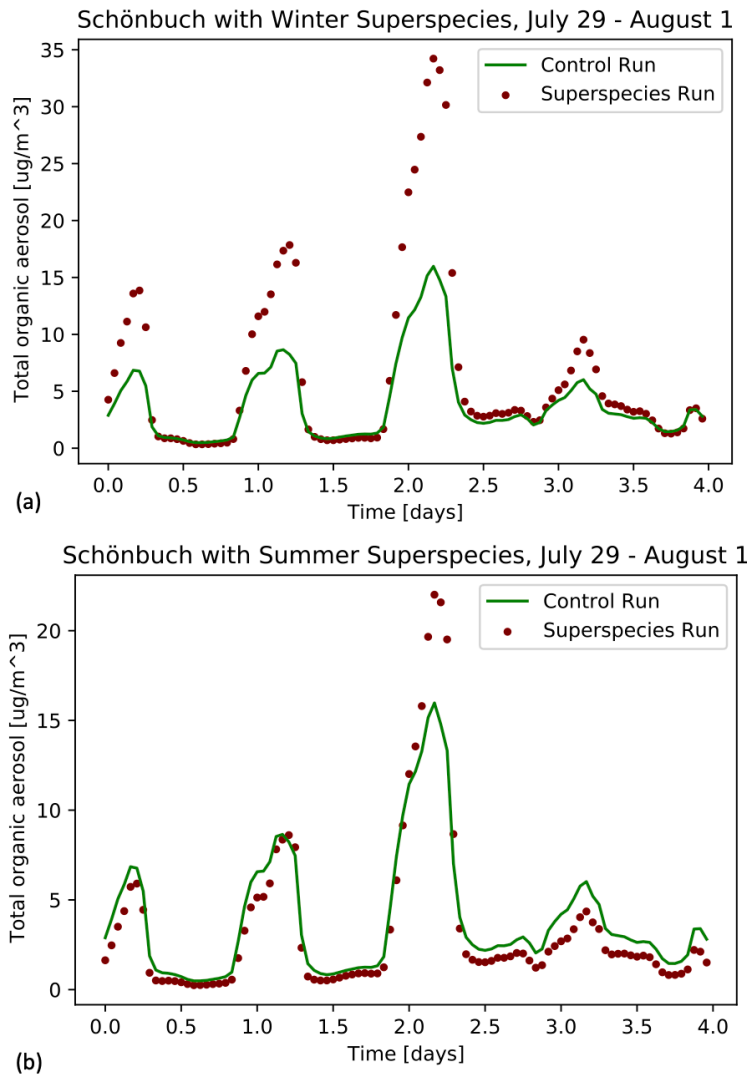


Figure 6. Temporal variation of TOA over Schönbuch from July 29th through August 1st using (a) winter-optimized superspecies and (b) summer-optimized species. The maroon points of TOA as predicted with when advecting superspecies are compared to the green line of TOA as modeled by the LE control run used as a baseline.

858 23rd through 28th, 2018, to obtain a superspecies parameterization optimized on
 859 summer conditions.

860 The superspecies approach optimized on summer conditions shows a much
 861 lower bias than the winter-optimized superspecies. The temporal behavior of
 862 summer-optimized superspecies from July 29th through August 1st after 10
 863 simulated days is shown in Figure 6b. Comparing Figure 6a to 6b, it can be seen
 864 that the spatiotemporal pattern of bSOA bias is addressed by using
 865 summer-optimized superspecies, which do not show the same nightly overestimation
 866 pattern of winter-optimized superspecies. Total bSOA is even slightly
 867 underestimated in the day when using summer-optimized superspecies.

868 Averaged over the entire domain and time period of July 29th through August
 869 1st, the summer-optimized superspecies display a slightly negative average bias for

870 bSOA of $-0.023 \mu\text{g m}^{-3}$. Small pockets of TOA overestimation (within $10 \mu\text{g m}^{-3}$)
871 still occur in the same regions as the winter-optimized superspecies: over highly
872 forested areas. The RMSE over the whole domain of time-averaged TOA was
873 $0.98 \mu\text{g m}^{-3}$ when using summer-optimized superspecies, less than half of the RMSE
874 of $2.12 \mu\text{g m}^{-3}$ when using winter-optimized superspecies. RMSE of the tracers
875 from the biogenic VBS (both gas and particle phases) for all times and grid cells is
876 reduced by a factor of 2, at $0.32 \mu\text{g m}^{-3}$ compared to $0.66 \mu\text{g m}^{-3}$. However, in
877 superspecies trained on either season, the biogenic VBS tracers in the summer show
878 significantly higher error than the tracers of the other VBS classes, with the siSOA
879 VBS class having the next highest RMSE value at $0.050 \mu\text{g m}^{-3}$. The limitation of
880 winter-optimized superspecies and the subsequent improvement in accuracy when
881 using summer-optimized superspecies indicates that this method might be best
882 applied to different seasons: creating seasonal-specific superspecies results in higher
883 accuracy. Analogously, Kelp et al. (2022) tested neural network surrogate models of
884 atmospheric chemistry optimized online for 3-month seasons against neural networks
885 trained online for a whole year, and concluded that ensembles of ML surrogate
886 models specialized for specific seasons improve accuracy and stability.

887 4.2 Towards Operational Forecasting on Higher-Resolution Domains

888 LOTOS-EUROS is one model in the ensemble used in the Copernicus
889 Atmospheric Modeling Service (CAM5) operational forecasts, which requires all
890 models to include SOA representation by 2023. The domain used in CAM5
891 operational forecasts has a higher resolution and wider domain than the domain
892 used by MACC: 0.1° by 0.1° for 420 by 700 grid cells compared to the 0.50° by 0.25°
893 used in the MACC domain, and extending past Moscow, Russia. The change of
894 resolution and domain increases the number of grid cells by a factor of 20. One
895 result of this is many more grid cells and computations. Another result is that the
896 operator splitting timestep Δt needs to decrease in order to satisfy the
897 Courant-Friedrichs-Lewy criterion as the grid cell distance is smaller. With a smaller
898 operator splitting timestep, the advection operator as well as the compression and
899 decompression steps are called more often. We investigate how the superspecies
900 approach, optimized on model output from February 20th through 24th on the
901 coarse-resolution MACC domain, generalizes to a 2 week run on the extended
902 high-resolution CAM5 domain. Figure 7 shows the time-averaged TOA
903 concentration across the entire CAM5 domain for the test period of February
904 25th-28th, 2018, chosen for ease of comparison with the winter run on the MACC
905 domain.

906 The superspecies run has a positive bias for TOA of $0.019 \mu\text{g m}^{-3}$, with visible
907 overestimation in the area near Moscow, Russia, which is not in the MACC grid
908 used to optimize the compression/decompression matrices. The colorbar limits of
909 Figure 7 (a), (b), and (c) were adjusted for visual comparison with Figure 4. For
910 this reason, colors at the upper or lower limits should be interpreted as greater or
911 equal to the limit. Though the maximum grid cell concentration of time-averaged
912 TOA from both the superspecies run and the control run was $28.2 \mu\text{g m}^{-3}$, 99.85%
913 of the grid cells had a time-averaged TOA under $7.6 \mu\text{g m}^{-3}$, which was chosen as
914 the upper limit of the colorbar. This means that only 0.15% of the grid cells in
915 Figures 7a and 7b exceed the limit shown in the colorbar. Neglecting the highest
916 0.15% of average TOA, the spatial patterns of the CAM5 control run in Figure 7a
917 are visually very similar to those of the that the CAM5 superspecies run in Figure
918 7b. Both show spatial patterns similar to the simulations performed on the MACC
919 grid for the same time period. The same approach is done for the bias shown in
920 Figure 7c, with very few grid cells in the CAM5 simulation exceeding the maximum
921 error of time-averaged TOA on the MACC grid. The maximum absolute error of
922 time-averaged TOA between the superspecies run and the control run was 8.9

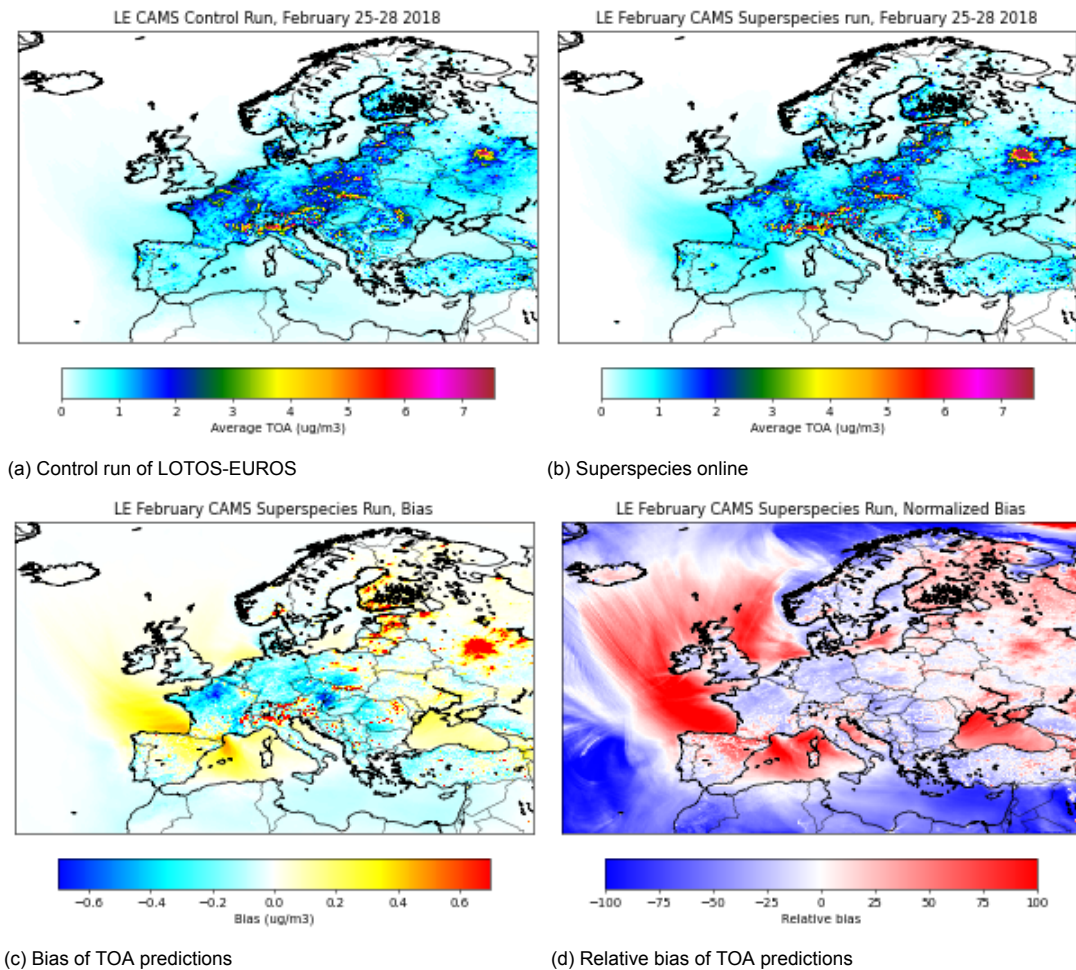


Figure 7. Time averaged TOA for the period of February 25th through 28th on the high-resolution domain used in CAMS operational forecasting, from control and superspecies runs, as well as bias and relative bias. The superspecies were optimized on model output from a simulation using the coarse-resolution MACC domain.

923 $\mu\text{g m}^{-3}$, but 99.2% of all grid cells had an absolute error of less than $0.70 \mu\text{g m}^{-3}$.
 924 Less than 1% of the grid cells in Figure 7c exceed the colorbar limit. The largest
 925 instantaneous bias for TOA was $89 \mu\text{g m}^{-3}$ at a grid cell in northwestern Spain near
 926 Ponferrada during a high TOA event on February 25th at 19:00. This grid cell also
 927 showed the highest time-averaged TOA concentration of $32.0 \mu\text{g m}^{-3}$ for the
 928 superspecies run, compared to $19.4 \mu\text{g m}^{-3}$ for the control run. At the highest
 929 positive bias of $89 \mu\text{g m}^{-3}$, TOA concentration as modeled by the superspecies run
 930 was $206.4 \mu\text{g m}^{-3}$ while the control run TOA concentration was $117.4 \mu\text{g m}^{-3}$.
 931 TOA during this event was composed almost wholly of primary material: the
 932 superspecies run modeled a POA concentration of $205.9 \mu\text{g m}^{-3}$ (99.78% of TOA
 933 concentration) while the control run POA concentration was $117.1 \mu\text{g m}^{-3}$ (99.75
 934 %). Rather than error compounding and leading to divergence from the control run,
 935 the superspecies run restabilized without error accumulation for the rest of the
 936 simulation: TOA concentration in the superspecies run converged to that of the
 937 control run.

938

4.3 Speed Improvement

939

940

941

942

943

944

945

946

947

948

949

950

951

952

953

954

955

The advection operator has an outer for-loop over all tracers that are transported. Using superspecies instead of VBS tracers reduces the number of passes through the outer for-loop. With the superspecies selected in Section 3, 16 superspecies (two gas and two particle superspecies for each of the four VBS classes) are advected rather than the 58 VBS tracers, reducing the total number of advected tracers from 104 to 62. The MACC run on the small domain was run sequentially on one computational node. Figure 8 shows wall time for the advection operator when advecting superspecies rather than VBS tracers was 6790 seconds, 56% of the time of (1.8 times faster than) the 12073 seconds to advect all tracers in the control run. The high resolution required for CAMS operational forecasts increases the computational intensity of the simulations which were performed using domain decomposition over 24 computing nodes with each node computing a subdomain of 175 by 70 grid cells. Using the VBS on the CAMS domain, advection wall time more than doubled from 34959 seconds to 74762 seconds. With superspecies advected instead of VBS tracers, wall time for the advection operator was then reduced to 49473 seconds. Advecting superspecies on the CAMS domain took about 66% of the time that advecting all the VBS tracers took, a speedup of approximately 1.5.

956

957

958

959

960

961

962

963

The timing results suggest that advection wall time depends linearly on number of tracers, which is expected behavior given the structure of the advection operator: an outer for-loop over all tracers. Compared to a run with no OA, inclusion of 58 VBS tracers increases the total number of advected tracers from 42 to 104 and more than doubles the computation time of the advection operator. Advecting 16 superspecies in place of 58 VBS tracers brings the total number of advected tracers down to 62: the proportion of 62/104 yields an expected 59% speed up, in between the speedup results on the MACC and CAMS domains.

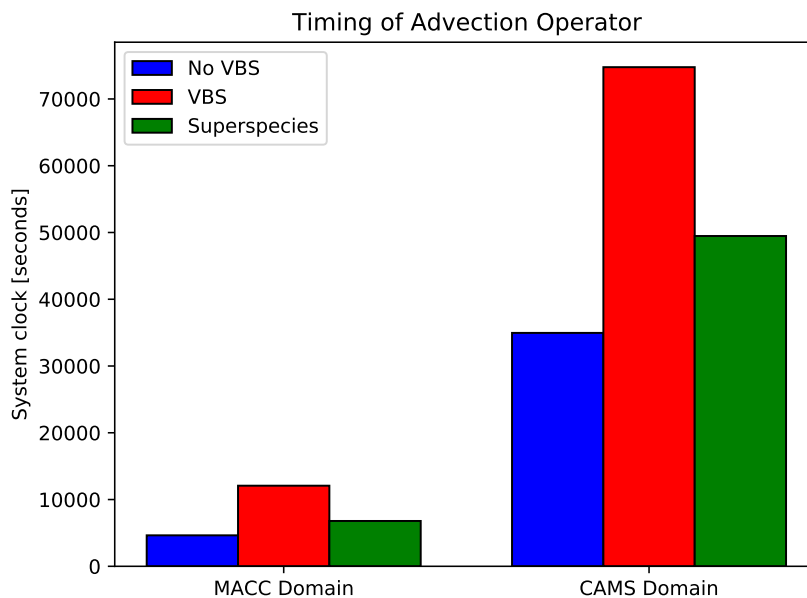


Figure 8. Use of the 58 VBS tracers approximately doubles the wall time spent on advection calculations. Advecting superspecies takes 56% and 66% of the time compared to advecting VBS tracers on the MACC and CAMS domains, respectively.

5 Conclusions

Modeling of organic aerosol processes via four VBS classes is high-dimensional and computationally expensive in LOTOS-EUROS v2.2.1, slowing the advection operator down by a factor of 2. This work developed data-driven methods to reduce the dimension of VBS tracers to a set of superspecies and reduce the computational burden on the advection operator. These methods were refined to ensure physical consistency, including semi-positive constraints, mass conservation, and information on phase. Multiple approaches were compared in Section 3 and non-negative matrix factorization additionally constrained to conserve mass and phase (Approach 4), after being evaluated on reconstruction accuracy and physical consistency, was selected to be implemented in LOTOS-EUROS v2.2.1 in Section 4. Approach 4 creates 16 phase-specific, class-specific superspecies, a compression factor of 3.6, while preserving phase and conserving total concentration to machine precision. The superspecies parameterization ran stably without runaway error for a model simulation of 2 weeks, exceeding the training time horizon. Higher bias of total OA concentration was shown when the superspecies, optimized to reconstruct winter OA patterns, were used for a 2 week run in the summer. During the summer run, the bias showed a clear spatiotemporal pattern, with biogenic SOA overestimated over forests at night. The superspecies were retrained on model output from summer conditions and implemented in LOTOS-EUROS v2.2.1 to reduce high bias. The results of this case study indicate that the superspecies might work best when optimized for season-specific conditions.

We found that the superspecies trained on the coarse-resolution MACC domain performed well when used on the fine-resolution domain used in CAMS operational forecasts for a period of 2 weeks. In an analysis period of 4 days performed at the end of the 2 week CAMS run, over 99% of all grid cells showed an absolute bias of time-averaged TOA within the maximum error of the MACC grid. Evaluating a grid cell that exceeded the maximum average error, we found that high overestimation of total OA concentration occurred at a high OA event, and converged back to the baseline simulation as time progressed rather than displaying continued error growth.

Advecting superspecies reduced the wall time spent on the advection operator: advecting superspecies took 56% to 66% of the time that it took to advect VBS tracers. Timing experiments indicate a linear dependence of wall time on number of tracers to advect, an expected relation from the structure of the advection operator, which uses a for-loop over all advected tracers. With linear dependence demonstrated, the design choice of compression factor (number of superspecies) can already give an estimate of theoretical speedup.

The use of physically consistent data-driven methods to find superspecies allows for inclusion of organic aerosol processes without doubling the computational burden on the advection operator. Though this approach has been demonstrated for 2-week forecasts on lower and higher resolutions, more work would have to be done to assess this method on longer timescales, including other seasons or seasonal transitions. This case study has not explored how the superspecies method might interface with other tracer compression methods such as the partitioning-based compression method in section 2.2, or how the superspecies may perform when used in other processes. However, preserving information on phase of the superspecies allows for their future use in phase-specific processes such as dry deposition, which can be computationally intensive in LOTOS-EUROS. Though demonstrated on organic aerosol species in a regional CTM as a case study, the focus of this approach on physical consistency and interpretability is relevant to other tracers, processes, and models. As physical consistency and computational efficiency are widely desired aspects of numerical modeling in the physical sciences, this approach

1017 could be adapted for use in comprehensive Earth system models with the purpose of
1018 providing forecasts of global atmospheric composition, for example GEOS-CF
1019 (Keller et al., 2021). More generally, this approach contributes additional physical
1020 consistency to a widely used dimensionality reduction technique (non-negative
1021 matrix factorization) that can be used to reversibly map between high and low
1022 detail in Earth system models.

1023 **Acknowledgments**

1024 This work was supported in part by the UC Davis CeDAR (Center for Data Science
1025 and Artificial Intelligence Research) Innovative Data Science Seed Funding Program.
1026 The authors thank Christoph Keller (NASA Goddard Space Flight Center) for
1027 valuable discussion throughout the project.

1028 **Open Research**

1029 The open source, most current version of LOTOS-EUROS is available online as
1030 detailed in Manders et al. (2017). The exact version of LOTOS-EUROS v2.2.1 used
1031 to generate the model output in this work, including the superspecies extension, as
1032 well as all Python code used for developing the data-driven approaches, analysis of
1033 model output, and figure generation, is available at Sturm (2022):
1034 <https://doi.org/10.5281/zenodo.6601166>.

1035 **References**

- 1036 Abadi, M., Agarwal, A., Barham, P., Brevdo, E., Chen, Z., Citro, C., ... Zheng,
1037 X. (2016). Tensorflow: A system for large-scale machine learning. In *12th*
1038 *{USENIX} symposium on operating systems design and implementation*
1039 *{OSDI} 16* (pp. 265–283).
- 1040 Bergström, R., Denier van der Gon, H. A. C., Prévôt, A. S. H., Yttri, K. E., &
1041 Simpson, D. (2012). Modelling of organic aerosols over europe (2002-
1042 2007) using a volatility basis set (vbs) framework: application of different
1043 assumptions regarding the formation of secondary organic aerosol. *Atmospheric*
1044 *Chemistry and Physics*, *12*(18), 8499–8527. Retrieved from [https://acp](https://acp.copernicus.org/articles/12/8499/2012/)
1045 [.copernicus.org/articles/12/8499/2012/](https://acp.copernicus.org/articles/12/8499/2012/) doi: 10.5194/acp-12-8499-2012
- 1046 Brasseur, G. P., & Jacob, D. J. (2017). *Modeling of atmospheric chemistry*.
1047 Cambridge University Press. doi: 10.1017/9781316544754
- 1048 Brenowitz, N. D., & Bretherton, C. S. (2019). Spatially extended tests of a neural
1049 network parametrization trained by coarse-graining. *Journal of Advances*
1050 *in Modeling Earth Systems*, *11*(8), 2728–2744. Retrieved from [https://](https://agupubs.onlinelibrary.wiley.com/doi/abs/10.1029/2019MS001711)
1051 agupubs.onlinelibrary.wiley.com/doi/abs/10.1029/2019MS001711 doi:
1052 <https://doi.org/10.1029/2019MS001711>
- 1053 Chollet, F., et al. (2015). *keras*.
- 1054 Ciarelli, G., Aksoyoglu, S., El Haddad, I., Bruns, E. A., Crippa, M., Poulain,
1055 L., ... Prévôt, A. S. H. (2017). Modelling winter organic aerosol at the
1056 european scale with camx: evaluation and source apportionment with a vbs
1057 parameterization based on novel wood burning smog chamber experiments.
1058 *Atmospheric Chemistry and Physics*, *17*(12), 7653–7669. Retrieved
1059 from <https://acp.copernicus.org/articles/17/7653/2017/> doi:
1060 [10.5194/acp-17-7653-2017](https://doi.org/10.5194/acp-17-7653-2017)
- 1061 Colette, A., Andersson, C., Manders, A., Mar, K., Mircea, M., Pay, M.-T., ... Wind,
1062 P. (2017). Eurodelta-trends, a multi-model experiment of air quality hindcast
1063 in europe over 1990–2010. *Geoscientific Model Development*, *10*(9), 3255–3276.
1064 Retrieved from <https://gmd.copernicus.org/articles/10/3255/2017/>
1065 doi: 10.5194/gmd-10-3255-2017
- 1066 Courant, R., Friedrichs, K., & Lewy, H. (1928, December). Über die partiellen
1067 Differenzgleichungen der mathematischen Physik. *Mathematische Annalen*,
1068 *100*(1), 32–74. Retrieved from <https://doi.org/10.1007/BF01448839> doi:
1069 [10.1007/BF01448839](https://doi.org/10.1007/BF01448839)
- 1070 Courant, R., Friedrichs, K., & Lewy, H. (1967). On the partial difference equations
1071 of mathematical physics. *IBM Journal of Research and Development*, *11*(2),
1072 215–234. doi: 10.1147/rd.112.0215
- 1073 de Gouw, J. A., Middlebrook, A. M., Warneke, C., Goldan, P. D., Kuster, W. C.,
1074 Roberts, J. M., ... Bates, T. S. (2005). Budget of organic carbon in a polluted

- 1075 atmosphere: Results from the new england air quality study in 2002. *Journal*
 1076 *of Geophysical Research: Atmospheres*, 110(D16). Retrieved from [https://](https://agupubs.onlinelibrary.wiley.com/doi/abs/10.1029/2004JD005623)
 1077 agupubs.onlinelibrary.wiley.com/doi/abs/10.1029/2004JD005623 doi:
 1078 <https://doi.org/10.1029/2004JD005623>
- 1079 Denier van der Gon, H. A. C., Bergström, R., Fountoukis, C., Johansson, C.,
 1080 Pandis, S. N., Simpson, D., & Visschedijk, A. J. H. (2015). Particulate
 1081 emissions from residential wood combustion in europe – revised estimates
 1082 and an evaluation. *Atmospheric Chemistry and Physics*, 15(11), 6503–6519.
 1083 Retrieved from <https://acp.copernicus.org/articles/15/6503/2015/>
 1084 doi: 10.5194/acp-15-6503-2015
- 1085 Donahue, N. M., Epstein, S. A., Pandis, S. N., & Robinson, A. L. (2011). A two-
 1086 dimensional volatility basis set: 1. organic-aerosol mixing thermodynamics.
 1087 *Atmospheric Chemistry and Physics*, 11(7), 3303–3318. Retrieved from
 1088 <https://acp.copernicus.org/articles/11/3303/2011/> doi: 10.5194/
 1089 acp-11-3303-2011
- 1090 Donahue, N. M., Henry, K. M., Mentel, T. F., Kiendler-Scharr, A., Spindler, C.,
 1091 Bohn, B., ... Baltensperger, U. (2012). Aging of biogenic secondary
 1092 organic aerosol via gas-phase oh radical reactions. *Proceedings of the*
 1093 *National Academy of Sciences*, 109(34), 13503-13508. Retrieved from
 1094 <https://www.pnas.org/doi/abs/10.1073/pnas.1115186109> doi:
 1095 10.1073/pnas.1115186109
- 1096 Donahue, N. M., Robinson, A., Stanier, C., & Pandis, S. (2006). Coupled
 1097 partitioning, dilution, and chemical aging of semivolatile organics.
 1098 *Environmental science & technology*, 40(8), 2635–2643.
- 1099 EEA. (2005). *Image2000 and clc2000. products and methods. corine land cover*
 1100 *updating for the year 2000*. Ispra Italy.
- 1101 Gery, M. W., Whitten, G. Z., Killus, J. P., & Dodge, M. C. (1989). A photochemical
 1102 kinetics mechanism for urban and regional scale computer modeling. *Journal*
 1103 *of Geophysical Research*, 94(D10), 12925. Retrieved from [http://doi.wiley](http://doi.wiley.com/10.1029/JD094iD10p12925)
 1104 [.com/10.1029/JD094iD10p12925](http://doi.wiley.com/10.1029/JD094iD10p12925) doi: 10.1029/JD094iD10p12925
- 1105 Hayes, P. L., Carlton, A. G., Baker, K. R., Ahmadov, R., Washenfelder, R. A.,
 1106 Alvarez, S., ... Jimenez, J. L. (2015). Modeling the formation and
 1107 aging of secondary organic aerosols in los angeles during calnex 2010.
 1108 *Atmospheric Chemistry and Physics*, 15(10), 5773–5801. Retrieved
 1109 from <https://acp.copernicus.org/articles/15/5773/2015/> doi:
 1110 10.5194/acp-15-5773-2015
- 1111 Heald, C. L., Jacob, D. J., Park, R. J., Russell, L. M., Huebert, B. J., Seinfeld,
 1112 J. H., ... Weber, R. J. (2005). A large organic aerosol source in the free
 1113 troposphere missing from current models. *Geophysical Research Letters*,
 1114 32(18). Retrieved from [https://agupubs.onlinelibrary.wiley.com/doi/](https://agupubs.onlinelibrary.wiley.com/doi/abs/10.1029/2005GL023831)
 1115 [abs/10.1029/2005GL023831](https://agupubs.onlinelibrary.wiley.com/doi/abs/10.1029/2005GL023831) doi: <https://doi.org/10.1029/2005GL023831>
- 1116 Hodzic, A., Kasibhatla, P. S., Jo, D. S., Cappa, C. D., Jimenez, J. L., Madronich,
 1117 S., & Park, R. J. (2016). Rethinking the global secondary organic
 1118 aerosol (soa) budget: stronger production, faster removal, shorter lifetime.
 1119 *Atmospheric Chemistry and Physics*, 16(12), 7917–7941. Retrieved
 1120 from <https://acp.copernicus.org/articles/16/7917/2016/> doi:
 1121 10.5194/acp-16-7917-2016
- 1122 Im, U., Bianconi, R., Solazzo, E., Kioutsioukis, I., Badia, A., Balzarini, A., ...
 1123 Galmarini, S. (2015). Evaluation of operational online-coupled regional
 1124 air quality models over europe and north america in the context of aqmeii
 1125 phase 2. part ii: Particulate matter. *Atmospheric Environment*, 115, 421-441.
 1126 Retrieved from [https://www.sciencedirect.com/science/article/pii/](https://www.sciencedirect.com/science/article/pii/S1352231014006839)
 1127 [S1352231014006839](https://www.sciencedirect.com/science/article/pii/S1352231014006839) doi: <https://doi.org/10.1016/j.atmosenv.2014.08.072>
- 1128 Janssen, R. H. H., Tsimpidi, A. P., Karydis, V. A., Pozzer, A., Lelieveld, J., Crippa,
 1129 M., ... Locoge, N. (2017). Influence of local production and vertical

- 1130 transport on the organic aerosol budget over paris. *Journal of Geophysical*
 1131 *Research: Atmospheres*, 122(15), 8276-8296. Retrieved from [https://](https://agupubs.onlinelibrary.wiley.com/doi/abs/10.1002/2016JD026402)
 1132 agupubs.onlinelibrary.wiley.com/doi/abs/10.1002/2016JD026402 doi:
 1133 <https://doi.org/10.1002/2016JD026402>
- 1134 Jathar, S. H., Gordon, T. D., Hennigan, C. J., Pye, H. O. T., Pouliot, G., Adams,
 1135 P. J., ... Robinson, A. L. (2014). Unspeciated organic emissions from
 1136 combustion sources and their influence on the secondary organic aerosol
 1137 budget in the united states. *Proceedings of the National Academy of Sciences*,
 1138 111(29), 10473-10478. Retrieved from [https://www.pnas.org/doi/abs/](https://www.pnas.org/doi/abs/10.1073/pnas.1323740111)
 1139 [10.1073/pnas.1323740111](https://www.pnas.org/doi/abs/10.1073/pnas.1323740111) doi: 10.1073/pnas.1323740111
- 1140 Jiang, J., Aksoyoglu, S., El-Haddad, I., Ciarelli, G., Denier van der Gon, H. A. C.,
 1141 Canonaco, F., ... Prévôt, A. S. H. (2019). Sources of organic aerosols
 1142 in europe: a modeling study using camx with modified volatility basis set
 1143 scheme. *Atmospheric Chemistry and Physics*, 19(24), 15247-15270. Retrieved
 1144 from <https://acp.copernicus.org/articles/19/15247/2019/> doi:
 1145 [10.5194/acp-19-15247-2019](https://doi.org/10.5194/acp-19-15247-2019)
- 1146 Jimenez, J. L., Canagaratna, M. R., Donahue, N. M., Prevot, A. S. H., Zhang,
 1147 Q., Kroll, J. H., ... Worsnop, D. R. (2009). Evolution of organic aerosols
 1148 in the atmosphere. *Science*, 326(5959), 1525-1529. Retrieved from
 1149 <https://www.science.org/doi/abs/10.1126/science.1180353> doi:
 1150 [10.1126/science.1180353](https://doi.org/10.1126/science.1180353)
- 1151 Kaiser, J. W., Heil, A., Andreae, M. O., Benedetti, A., Chubarova, N., Jones, L.,
 1152 ... van der Werf, G. R. (2012). Biomass burning emissions estimated
 1153 with a global fire assimilation system based on observed fire radiative
 1154 power. *Biogeosciences*, 9(1), 527-554. Retrieved from [http://www](http://www.biogeosciences.net/9/527/2012/bg-9-527-2012-discussion.html)
 1155 [.biogeosciences.net/9/527/2012/bg-9-527-2012-discussion.html](http://www.biogeosciences.net/9/527/2012/bg-9-527-2012-discussion.html) doi:
 1156 [10.5194/bg-9-527-2012](https://doi.org/10.5194/bg-9-527-2012)
- 1157 Keller, C. A., Knowland, K. E., Duncan, B. N., Liu, J., Anderson, D. C., Das, S., ...
 1158 Pawson, S. (2021). Description of the nasa geos composition forecast modeling
 1159 system geos-cf v1.0. *Journal of Advances in Modeling Earth Systems*, 13(4),
 1160 e2020MS002413. Retrieved from [https://agupubs.onlinelibrary.wiley](https://agupubs.onlinelibrary.wiley.com/doi/abs/10.1029/2020MS002413)
 1161 [.com/doi/abs/10.1029/2020MS002413](https://agupubs.onlinelibrary.wiley.com/doi/abs/10.1029/2020MS002413) (e2020MS002413 2020MS002413) doi:
 1162 <https://doi.org/10.1029/2020MS002413>
- 1163 Kelp, M. M., Jacob, D. J., Kutz, J. N., Marshall, J. D., & Tessum, C. W.
 1164 (2020). Toward stable, general machine-learned models of the atmospheric
 1165 chemical system. *Journal of Geophysical Research: Atmospheres*, 125(23),
 1166 e2020JD032759. Retrieved from [https://agupubs.onlinelibrary.wiley](https://agupubs.onlinelibrary.wiley.com/doi/abs/10.1029/2020JD032759)
 1167 [.com/doi/abs/10.1029/2020JD032759](https://agupubs.onlinelibrary.wiley.com/doi/abs/10.1029/2020JD032759) (e2020JD032759 2020JD032759) doi:
 1168 <https://doi.org/10.1029/2020JD032759>
- 1169 Kelp, M. M., Jacob, D. J., Lin, H., & Sulprizio, M. P. (2022). An online-learned
 1170 neural network chemical solver for stable long-term global simulations of
 1171 atmospheric chemistry. *Journal of Advances in Modeling Earth Systems*, 14(6),
 1172 e2021MS002926. Retrieved from [https://agupubs.onlinelibrary.wiley](https://agupubs.onlinelibrary.wiley.com/doi/abs/10.1029/2021MS002926)
 1173 [.com/doi/abs/10.1029/2021MS002926](https://agupubs.onlinelibrary.wiley.com/doi/abs/10.1029/2021MS002926) (e2021MS002926 2021MS002926) doi:
 1174 <https://doi.org/10.1029/2021MS002926>
- 1175 Kelp, M. M., Tessum, C. W., & Marshall, J. D. (2018). Orders-of-magnitude
 1176 speedup in atmospheric chemistry modeling through neural network-based
 1177 emulation. *arXiv preprint arXiv:1808.03874*.
- 1178 Knote, C., Hodzic, A., & Jimenez, J. L. (2015). The effect of dry and wet
 1179 deposition of condensable vapors on secondary organic aerosols concentrations
 1180 over the continental us. *Atmospheric Chemistry and Physics*, 15(1), 1-18.
 1181 Retrieved from <https://acp.copernicus.org/articles/15/1/2015/> doi:
 1182 [10.5194/acp-15-1-2015](https://doi.org/10.5194/acp-15-1-2015)
- 1183 Köble, R., & Seufert, G. (2001). Novel maps for forest tree species in europe. In
 1184 *Proceedings of the 8th european symposium on the physico-chemical behaviour*

- 1185 of air pollutants: “a changing atmosphere (pp. 17–20).
- 1186 Lane, T. E., Donahue, N. M., & Pandis, S. N. (2008). Effect of no x on secondary
1187 organic aerosol concentrations. *Environmental science & technology*, 42(16),
1188 6022–6027.
- 1189 Lee, D. D., & Seung, H. S. (1999). Learning the parts of objects by non-negative
1190 matrix factorization. *Nature*, 401(6755), 788–791.
- 1191 Li, M., Soltanolkotabi, M., & Oymak, S. (2020, 26–28 Aug). Gradient descent with
1192 early stopping is provably robust to label noise for overparameterized neural
1193 networks. In S. Chiappa & R. Calandra (Eds.), *Proceedings of the twenty third
1194 international conference on artificial intelligence and statistics* (Vol. 108, pp.
1195 4313–4324). PMLR. Retrieved from [https://proceedings.mlr.press/v108/
1196 li20j.html](https://proceedings.mlr.press/v108/li20j.html)
- 1197 Liao, H., Henze, D. K., Seinfeld, J. H., Wu, S., & Mickley, L. J. (2007). Biogenic
1198 secondary organic aerosol over the united states: Comparison of climatological
1199 simulations with observations. *Journal of Geophysical Research: Atmospheres*,
1200 112(D6).
- 1201 Lu, Q., Murphy, B. N., Qin, M., Adams, P. J., Zhao, Y., Pye, H. O. T., ...
1202 Robinson, A. L. (2020). Simulation of organic aerosol formation during
1203 the calnex study: updated mobile emissions and secondary organic aerosol
1204 parameterization for intermediate-volatility organic compounds. *Atmospheric
1205 Chemistry and Physics*, 20(7), 4313–4332. Retrieved from [https://acp
1206 .copernicus.org/articles/20/4313/2020/](https://acp.copernicus.org/articles/20/4313/2020/) doi: 10.5194/acp-20-4313-2020
- 1207 Manders, A. M. M., Bultjes, P. J. H., Curier, L., Denier van der Gon, H. A. C.,
1208 Hendriks, C., Jonkers, S., ... Schaap, M. (2017). Curriculum vitae of
1209 the lotos-euros (v2.0) chemistry transport model. *Geoscientific Model
1210 Development*, 10(11), 4145–4173. Retrieved from [https://gmd.copernicus
1211 .org/articles/10/4145/2017/](https://gmd.copernicus.org/articles/10/4145/2017/) doi: 10.5194/gmd-10-4145-2017
- 1212 Manders-Groot, A. M. M., Segers, A. J., & Jonkers, S. (2021). Lotos-euros v2.2.000
1213 reference guide. *TNO Reports*.
- 1214 Marais, E. A., Jacob, D. J., Jimenez, J. L., Campuzano-Jost, P., Day, D. A., Hu,
1215 W., ... McNeill, V. F. (2016). Aqueous-phase mechanism for secondary
1216 organic aerosol formation from isoprene: application to the southeast united
1217 states and co-benefit of so₂ emission controls. *Atmospheric Chemistry and
1218 Physics*, 16(3), 1603–1618. Retrieved from [https://acp.copernicus.org/
1219 articles/16/1603/2016/](https://acp.copernicus.org/articles/16/1603/2016/) doi: 10.5194/acp-16-1603-2016
- 1220 Marsland, S. (2014). *Machine learning: An algorithmic perspective, second edition*
1221 (2nd ed.). Chapman & Hall/CRC.
- 1222 Matsui, H. (2017). Development of a global aerosol model using a two-dimensional
1223 sectional method: 1. model design. *Journal of Advances in Modeling Earth
1224 Systems*, 9(4), 1921–1947.
- 1225 Mircea, M., Bessagnet, B., D’Isidoro, M., Pirovano, G., Aksoyoglu, S., Ciarelli, G.,
1226 ... others (2019). Eurodelta iii exercise: An evaluation of air quality models’
1227 capacity to reproduce the carbonaceous aerosol. *Atmospheric Environment: X*,
1228 2, 100018.
- 1229 Murphy, B. N., Donahue, N. M., Fountoukis, C., Dall’Osto, M., O’Dowd, C.,
1230 Kiendler-Scharr, A., & Pandis, S. N. (2012). Functionalization and
1231 fragmentation during ambient organic aerosol aging: application of the 2-
1232 d volatility basis set to field studies. *Atmospheric Chemistry and Physics*,
1233 12(22), 10797–10816.
- 1234 Murphy, B. N., & Pandis, S. N. (2009). Simulating the formation of semivolatile
1235 primary and secondary organic aerosol in a regional chemical transport model.
1236 *Environmental science & technology*, 43(13), 4722–4728.
- 1237 Nagori, J., Janssen, R. H. H., Fry, J. L., Krol, M., Jimenez, J. L., Hu, W., & Vilà-
1238 Guerau de Arellano, J. (2019). Biogenic emissions and land-atmosphere
1239 interactions as drivers of the daytime evolution of secondary organic aerosol

- 1240 in the southeastern us. *Atmospheric Chemistry and Physics*, *19*(2), 701–729.
 1241 Retrieved from <https://acp.copernicus.org/articles/19/701/2019/> doi:
 1242 10.5194/acp-19-701-2019
- 1243 Ng, N. L., Kroll, J. H., Keywood, M. D., Bahreini, R., Varutbangkul, V., Flagan,
 1244 R. C., ... Goldstein, A. H. (2006). Contribution of first-versus second-
 1245 generation products to secondary organic aerosols formed in the oxidation
 1246 of biogenic hydrocarbons. *Environmental science & technology*, *40*(7), 2283–
 1247 2297.
- 1248 O’Dowd, C., Ceburnis, D., Ovadnevaite, J., Vaishya, A., Rinaldi, M., & Facchini, M.
 1249 (2014). Do anthropogenic, continental or coastal aerosol sources impact on a
 1250 marine aerosol signature at mace head? *Atmospheric Chemistry and Physics*,
 1251 *14*(19), 10687–10704.
- 1252 Ots, R., Young, D. E., Vieno, M., Xu, L., Dunmore, R. E., Allan, J. D., ... Heal,
 1253 M. R. (2016). Simulating secondary organic aerosol from missing diesel-related
 1254 intermediate-volatility organic compound emissions during the clean air for
 1255 london (clearflo) campaign. *Atmospheric Chemistry and Physics*, *16*(10),
 1256 6453–6473. Retrieved from [https://acp.copernicus.org/articles/16/](https://acp.copernicus.org/articles/16/6453/2016/)
 1257 [6453/2016/](https://acp.copernicus.org/articles/16/6453/2016/) doi: 10.5194/acp-16-6453-2016
- 1258 Paatero, P., & Tapper, U. (1994). Positive matrix factorization: A non-negative
 1259 factor model with optimal utilization of error estimates of data values.
 1260 *Environmetrics*, *5*(2), 111–126.
- 1261 Pai, S. J., Heald, C. L., Pierce, J. R., Farina, S. C., Marais, E. A., Jimenez, J. L.,
 1262 ... Vu, K. (2020). An evaluation of global organic aerosol schemes using
 1263 airborne observations. *Atmospheric Chemistry and Physics*, *20*(5), 2637–2665.
 1264 Retrieved from <https://acp.copernicus.org/articles/20/2637/2020/>
 1265 doi: 10.5194/acp-20-2637-2020
- 1266 Pedregosa, F., Varoquaux, G., Gramfort, A., Michel, V., Thirion, B., Grisel, O., ...
 1267 Duchesnay, E. (2011). Scikit-learn: Machine learning in Python. *Journal of*
 1268 *Machine Learning Research*, *12*, 2825–2830.
- 1269 Pye, H. O. T., Murphy, B. N., Xu, L., Ng, N. L., Carlton, A. G., Guo, H., ...
 1270 Goldstein, A. H. (2017). On the implications of aerosol liquid water and phase
 1271 separation for organic aerosol mass. *Atmospheric Chemistry and Physics*,
 1272 *17*(1), 343–369. Retrieved from [https://acp.copernicus.org/articles/17/](https://acp.copernicus.org/articles/17/343/2017/)
 1273 [343/2017/](https://acp.copernicus.org/articles/17/343/2017/) doi: 10.5194/acp-17-343-2017
- 1274 Pye, H. O. T., Pinder, R. W., Piletic, I. R., Xie, Y., Capps, S. L., Lin, Y.-H.,
 1275 ... Edney, E. O. (2013). Epoxide pathways improve model predictions
 1276 of isoprene markers and reveal key role of acidity in aerosol formation.
 1277 *Environmental Science & Technology*, *47*(19), 11056–11064. Retrieved
 1278 from <https://doi.org/10.1021/es402106h> (PMID: 24024583) doi:
 1279 10.1021/es402106h
- 1280 Rasp, S. (2020). Coupled online learning as a way to tackle instabilities and biases
 1281 in neural network parameterizations: general algorithms and lorenz 96 case
 1282 study (v1. 0). *Geoscientific Model Development*, *13*(5), 2185–2196.
- 1283 Rasp, S., Pritchard, M. S., & Gentine, P. (2018). Deep learning to represent subgrid
 1284 processes in climate models. *Proceedings of the National Academy of Sciences*,
 1285 *115*(39), 9684–9689.
- 1286 Robinson, A. L., Donahue, N. M., Shrivastava, M. K., Weitkamp, E. A., Sage,
 1287 A. M., Grieshop, A. P., ... Pandis, S. N. (2007). Rethinking organic aerosols:
 1288 Semivolatile emissions and photochemical aging. *Science*, *315*(5816), 1259–
 1289 1262.
- 1290 Schreck, J. S., Becker, C., Gagne, D. J., Lawrence, K., Wang, S., Mouchel-Vallon,
 1291 C., ... Hodzic, A. (2022). Neural network emulation of the formation of
 1292 organic aerosols based on the explicit gecko-a chemistry model. *Journal of*
 1293 *Advances in Modeling Earth Systems*, *n/a*(n/a), e2021MS002974. Retrieved
 1294 from <https://agupubs.onlinelibrary.wiley.com/doi/abs/10.1029/>

- 1295 2021MS002974 (e2021MS002974 2021MS002974) doi: <https://doi.org/10.1029/2021MS002974>
 1296
- 1297 Seinfeld, J. H., & Pandis, S. N. (2006). *Atmospheric chemistry and physics : from*
 1298 *air pollution to climate change*. Hoboken, N.J. J. Wiley.
- 1299 Shrivastava, M. K., Lane, T. E., Donahue, N. M., Pandis, S. N., & Robinson, A. L.
 1300 (2008). Effects of gas particle partitioning and aging of primary emissions on
 1301 urban and regional organic aerosol concentrations. *Journal of Geophysical*
 1302 *Research: Atmospheres*, 113(D18).
- 1303 Sturm, P. O. (2021). Advecting superspecies: Reduced order modeling of organic
 1304 aerosols in lotos-euros using machine learning. *TU Delft Education Repository*.
 1305 Retrieved from [http://resolver.tudelft.nl/uuid:2c3be50e-5340-4495](http://resolver.tudelft.nl/uuid:2c3be50e-5340-4495-a0b7-1670db9be329)
 1306 [-a0b7-1670db9be329](http://resolver.tudelft.nl/uuid:2c3be50e-5340-4495-a0b7-1670db9be329)
- 1307 Sturm, P. O. (2022). Code for sturm et al. advecting superspecies. [Software].
 1308 *Zenodo*. Retrieved from <https://doi.org/10.5281/zenodo.6601166>
- 1309 Sturm, P. O., & Wexler, A. S. (2020). A mass- and energy-conserving framework
 1310 for using machine learning to speed computations: a photochemistry
 1311 example. *Geoscientific Model Development*, 13(9), 4435–4442. Retrieved
 1312 from <https://gmd.copernicus.org/articles/13/4435/2020/> doi:
 1313 10.5194/gmd-13-4435-2020
- 1314 Sturm, P. O., & Wexler, A. S. (2022). Conservation laws in a neural network
 1315 architecture: enforcing the atom balance of a julia-based photochemical model
 1316 (v0.2.0). *Geoscientific Model Development*, 15(8), 3417–3431. Retrieved
 1317 from <https://gmd.copernicus.org/articles/15/3417/2022/> doi:
 1318 10.5194/gmd-15-3417-2022
- 1319 Theodoritsi, G. N., & Pandis, S. N. (2019). Simulation of the chemical evolution of
 1320 biomass burning organic aerosol. *Atmospheric Chemistry and Physics*, 19(8),
 1321 5403–5415. Retrieved from [https://acp.copernicus.org/articles/19/](https://acp.copernicus.org/articles/19/5403/2019/)
 1322 [5403/2019/](https://acp.copernicus.org/articles/19/5403/2019/) doi: 10.5194/acp-19-5403-2019
- 1323 Timmermans, R., van Pinxteren, D., Kranenburg, R., Hendriks, C., Fomba, K.,
 1324 Herrmann, H., & Schaap, M. (2022). Evaluation of modelled lotos-euros with
 1325 observational based pm10 source attribution. *Atmospheric Environment:*
 1326 *X*, 14, 100173. Retrieved from [https://www.sciencedirect.com/](https://www.sciencedirect.com/science/article/pii/S2590162122000272)
 1327 [science/article/pii/S2590162122000272](https://www.sciencedirect.com/science/article/pii/S2590162122000272) doi: [https://doi.org/10.1016/](https://doi.org/10.1016/j.aeaoa.2022.100173)
 1328 [j.aeaoa.2022.100173](https://doi.org/10.1016/j.aeaoa.2022.100173)
- 1329 Tsimpidi, A. P., Karydis, V. A., Pozzer, A., Pandis, S. N., & Lelieveld, J. (2014).
 1330 Oracle (v1. 0): module to simulate the organic aerosol composition and
 1331 evolution in the atmosphere. *Geoscientific Model Development*, 7(6), 3153–
 1332 3172.
- 1333 Tsimpidi, A. P., Karydis, V. A., Zavala, M., Lei, W., Molina, L., Ulbrich, I. M.,
 1334 ... Pandis, S. N. (2010). Evaluation of the volatility basis-set approach for
 1335 the simulation of organic aerosol formation in the mexico city metropolitan
 1336 area. *Atmospheric Chemistry and Physics*, 10(2), 525–546. Retrieved
 1337 from <https://acp.copernicus.org/articles/10/525/2010/> doi:
 1338 10.5194/acp-10-525-2010
- 1339 Walcek, C. J. (2000). Minor flux adjustment near mixing ratio extremes for
 1340 simplified yet highly accurate monotonic calculation of tracer advection.
 1341 *Journal of Geophysical Research: Atmospheres*, 105(D7), 9335–9348.
- 1342 Yuval, J., O’Gorman, P. A., & Hill, C. N. (2021). Use of neural networks for stable,
 1343 accurate and physically consistent parameterization of subgrid atmospheric
 1344 processes with good performance at reduced precision. *Geophysical Research*
 1345 *Letters*, 48(6), e2020GL091363.
- 1346 Zanten, M. v., Sauter, F., Wichink Kruit, R., Jaarsveld, J. v., Pul, W. v., &
 1347 Wichink Kruit, R. (2010). *Description of the DEPAC module. Dry deposition*
 1348 *modelling with DEPAC.GCN2010* (Tech. Rep.). Bilthoven, The Netherlands:
 1349 Rijksinstituut voor volksgezondheid en Milieu, RIVM report 680180001.

- 1350 Retrieved from http://www.rivm.nl/Documenten_en_publicaties/
1351 Wetenschappelijk/Rapporten/2010/oktober/Description_of_the_DEPAC
1352 _module_Dry_deposition_modelling_with_DEPAC_GCN2010
1353 Zhang, L. (2001). A size-segregated particle dry deposition scheme for an
1354 atmospheric aerosol module. *Atmospheric Environment*, 35(3), 549–560.
1355 Retrieved from [http://www.sciencedirect.com/science/article/pii/](http://www.sciencedirect.com/science/article/pii/S1352231000003265)
1356 S1352231000003265 doi: 10.1016/S1352-2310(00)00326-5
1357 Zhao, B., Shrivastava, M., Donahue, N. M., Gordon, H., Schervish, M., Shilling,
1358 J. E., ... Fast, J. D. (2020). High concentration of ultrafine particles in
1359 the amazon free troposphere produced by organic new particle formation.
1360 *Proceedings of the National Academy of Sciences*, 117(41), 25344–25351.